Modulation of tropical cyclogenesis on subseasonal-to-interannual timescales in the deep-learning climate emulator ACE2

Mu-Ting Chien1, Elizabeth A. Barnes1 and Eric D. Maloney1
1 Department of Atmospheric Science, Colorado State University, Fort Collins, USA

E-mail: Mu-Ting.Chien@colostate.edu

Submitted to a peer-reviewed journal *IOP Machine Learning: Earth* on April 26, 2025.

IOP Publishing Machine Learning: Earth
Journal **XX** (XXXX) XXXXXX https://doi.org/XXXX/XXXX

Modulation of tropical cyclogenesis on subseasonal-to-interannual timescales in the deep-learning climate emulator ACE2

Mu-Ting Chien[1], Elizabeth A. Barnes[1] and Eric D. Maloney[1]

[1] Department of Atmospheric Science, Colorado State University, Fort Collins, USA

E-mail: Mu-Ting.Chien@colostate.edu

Received April 26, 2025
Accepted for publication xxxxxx
Published xxxxxx

Abstract

Deep-learning global climate emulators are providing a new lens to investigate tropical cyclogenesis (TC genesis). However, without explicitly enforcing known physics, it is necessary to assess whether TC genesis in these models is physical. To address this question, we use the Ai2 Climate Emulator version 2 (ACE2) trained on ERA5 reanalysis to investigate TC genesis and its relationship with the large-scale environment on subseasonal-to-interannual timescales. We run simulations with ACE2 using forcing fields from 2001 to 2010, which is outside of its training period. Compared to observations, the geographic distribution and annual cycle of TC genesis are reasonably represented in ACE2 across the globe. TC genesis in ACE2 generally occurs with favorable environmental conditions (high genesis potential index) on annual, interannual, and subseasonal timescales. On subseasonal timescales, ACE2 shows that the environmental conditions for TC genesis are affected by the occurrence of the Madden-Julian Oscillation (MJO) and convectively coupled equatorial waves (CCEWs), as in observations. With pronounced eastward propagation of the MJO and realistic simulation of precipitation and three-dimensional circulation anomalies in ACE2, a clear signal of MJO modulation of TC genesis is found in most basins. This study suggests that deep learning climate emulators may be a useful tool for understanding cyclogenesis in the current climate from subseasonal-to-interannual timescales, as well as their changes in altered climates.

Keywords: tropical cyclogenesis, Madden-Julian Oscillation, subseasonal variability, deep-learning climate emulator

1. Introduction

Tropical cyclones (TCs) cause significant economic and societal impacts during and after landfall, with around eighty TCs occurring annually across the globe. However, there are no agreed-upon explanations for this global frequency (e.g., Sobel et al. 2021), highlighting that the processes contributing to tropical cyclone formation (TC genesis) are not fully understood.

The frequency of TC genesis varies on different timescales. On the annual timescale, most basins exhibit TC genesis during the summer seasons (e.g., Yang et al. 2021). On interannual timescales, TC frequency is affected by the El Nino-Southern Oscillation (ENSO) and other modes of variability (e.g., Carmargo et al. 2007a). On subseasonal timescales (2 weeks to ~3 months), TC frequency is modulated by the Madden-Julian Oscillation (MJO) and convectively coupled equatorial waves (CCEWs) (e.g., Maloney and Hartmann 2000; Carmargo et al. 2009; Schreck et al. 2012; Wu and Takahashi 2018; Feng et al. 2023; Rios-Berrios et al. 2024).

On even longer timescales, the change in TC frequency in response to global warming is still an ongoing debate (e.g., Yoshida et al. 2017; Roberts et al. 2020; Yamada et al. 2021). While global climate models are the most common tools to investigate this question, many of them struggle to represent

TC frequency realistically in the current climate. For example, the most up-to-date high-resolution global climate (high-res-MIP) models simulate annual TC numbers ranging from 10 to 120 (e.g., Roberts et al. 2020). Further, some models predict a decrease in TC frequency, while other models predict an increase under warming scenarios of the 21st Century (e.g., Yoshida et al. 2017; Roberts et al. 2020; Yamada et al. 2021). While these differences in TC response to warming could come from differences in model parameterization schemes, their dynamical cores, and other assumptions of the models, it has been hard to pinpoint the exact reason for these model deficiencies (e.g., Roberts et al. 2020). This discrepancy highlights room for improvement in understanding TC genesis and its relationship with the large-scale environment.

The controls on TC genesis have been an active research question since the 1970s. Gray (1975) proposed general conditions favorable for TC genesis, including high sea surface temperature, low vertical wind shear, and pre-existing vorticity. These environmental conditions can be modified geographically, influenced by seasonal cycles, and altered by various weather and climate variability (e.g., ENSO, MJO, CCEWs). Based on this, past work has developed genesis potential indices to quantify how favorable the environment is to TC genesis on annual, interannual, and subseasonal timescales (e.g., Emanuel and Nolan 2004; Carmargo et al. 2007b; Tippett et al. 2011). Although these genesis potential indices are positively correlated with the actual TC genesis from subseasonal-to-interannual timescales to first order, there are also scenarios in which the indices are not enough to predict actual TC genesis (e.g., Yang et al. 2021; Emlaw and Kim 2024). Nevertheless, quantifying genesis potential indices is a first step when investigating TC genesis.

In recent years, new advances in deep-learning models have provided promise for making progress on cyclogenesis. For example, several deep-learning weather and/or climate emulators (AI models) have been developed, such as Pangu-Weather (Bi et al. 2022; 2023), FourCastNet (Pathak et al. 2022; Kurth et al. 2023), GraphCast (Lam et al. 2022), ACE (Watts-Mayer et al. 2023; 2024), DLWP (Weyn et al. 2019; Weyn et al. 2021; Cresswell-Clay et al. 2024), and many more. These models are often trained on climate model output or reanalysis products. Hence, these models are often called weather or climate "emulators". Among these emulators, some are stable enough to run for hundreds to thousands of years (e.g., ACE and DLWP), making it possible to conduct climate simulations similar to what has been done for decades using the conventional dynamics-based general circulation models (GCMs). Furthermore, these AI models can be run efficiently, requiring many fewer computational resources compared to traditional GCMs. These AI climate models provide a unique opportunity to investigate TC genesis and its sensitivity to environmental conditions on various timescales. Using large amounts of data (e.g., large ensembles) generated from the AI emulators could potentially improve understanding of the relationships between TC genesis and the large-scale environment, which are difficult to learn using limited observations or some conventional GCMs due to their struggles in accurately representing the climatology of TCs.

One challenge, however, is that it is unknown to what extent we can trust the realism of TC genesis in AI models, given that these models do not explicitly encode physical equations as is often done in traditional GCMs. In addition, the resolution of these AI models is usually coarse (1 degree or larger) compared to the most up-to-date high-resolution climate models or cloud-resolving simulations, making it difficult to represent the mesoscale processes that influence TC genesis explicitly. However, the data-driven approach (i.e. learning relationships between data) could allow for learning subgrid processes and representing them at larger scales without explicitly simulating them.

No studies have comprehensively examined TC genesis in AI models to our knowledge. Recent studies have highlighted that the TC track forecast skill in AI models can be comparable to or better than that of the dynamical models, while the intensity forecast in AI models is poor (DeMaria et al. 2024). This is likely because TC track is dominated by the large-scale environment, while the intensity forecast relies on the convective-scale processes within TC inner core. Regarding the inner core TC structures in AI models, Bonavita (2024) found an unphysical relationship between zonal wind, divergence, and vertical velocity. These results suggest that AI models may perform better when the large-scale environment dominates, and the convective-scale processes are secondary.

Since large-scale environmental conditions likely strongly affect TC genesis, AI models may be good tools to investigate TC genesis. This study tests the hypothesis that on particular AI model (ACE2) can realistically capture the relationship between TC genesis and the large-scale environment from subseasonal-to-interannual timescale. We create an ensemble ACE2 simulations using sea-surface temperatures from 2001 to 2010 and comprehensively examine the modulation of TC genesis by the large-scale environment, including the seasonal cycle, interannual variability, and the MJO. Environmental conditions are diagnosed based on a genesis potential index of Tippett et al. (2011). We systematically document the relationships between TC genesis and genesis potential index in the AI simulations from subseasonal-to-interannual timescale. The relationships are compared with those from reanalysis and observations, serving for verification of whether AI models simulate TC genesis reasonably. The remaining paper is structured as follows: Section 2 describes the AI simulations and the verification data from observations and reanalysis. Section 3 presents the results of TC genesis and the environment on multiple timescales. Section 4 concludes our findings, discusses the implications, and proposes possible directions for leveraging AI models for future research on TC genesis.

2. Method

2.1 ACE2-ERA5 simulations

We use the Ai2 Climate Emulator version 2 (ACE2) to perform annual simulations of the present-day climate (Watts-Mayer et al. 2024). Specifically, we utilize the version of ACE2 trained on ERA5 reanalysis (Hersbach et al. 2020) (ACE2-ERA hereafter). ACE2-ERA5 predicts fields of atmospheric variables, including temperature, humidity, zonal wind, meridional wind, precipitation, and surface pressure for each 6-hour model timestep via autoregressive integration. The model is forced by the observed daily sea surface temperature and annually-varying greenhouse gases. The model architecture is based on a Spherical Fourier Neural Operator (SFNO) architecture (Bonev et al. 2023). The horizontal resolution of the model is 1-deg, with eight vertical levels on the sigma-pressure-hybrid coordinate. Extensive details about the ACE2-ERA5 model can be found in the original paper (Watt-Mayer et al. 2024).

We perform two sets of simulations. The first simulation (Simulation I) is initialized on Jan 1, 2001, and integrated for 10 years with prescribed sea surface temperatures and greenhouse gases from 2001 to 2010. The period of 2001 to 2010 is chosen because it is outside of the ACE2-ERA5 training period. We compare the simulation with observations and ERA5 to verify the ability of ACE2-ERA5 to represent TC genesis with fidelity.

Observations represent just one realization of the underlying environment. Under the same large-scale environmental forcings, small perturbations in initial conditions could lead to differences in the day-to-day variations of the atmosphere. To capture a wider range of outcomes for the same SST and greenhouse gas forcings, we run a second set of simulations (Simulation II) with 10 ensemble members. We obtain ten members by repeating perpetual forcings for each year between 2001 and 2010 10 times. Specifically, we initialize the simulation on Jan 1, 2001 from ERA5 reanalysis and run repeating forcings of 2001 ten times. We then repeat this procedure for 2002 forcings, etc. This process is repeated until 10 years of simulation under each of the forcing years are complete, providing us with a total of 100 simulated years. We use perpetual forcings to generate ensemble members because it is easier to implement based on how the model code is written. We suspect our results are qualitatively similar to running continuous forcings from 2001 to 2010 with 10 different initial conditions.

2.2 Observation and reanalysis data

To validate our ACE2-ERA5 simulations, we use ERA5 reanalysis (Hersbach et al. 2020) for field variables such as temperature, humidity, zonal wind, meridional wind, and sea level pressure. For precipitation, we use the GPM IMERG satellite-observed precipitation (Huffman et al. 2020). Note that satellite-observed precipitation is used instead of ERA5 precipitation because subseasonal precipitation variability is underestimated in ERA5 than in satellite observations (e.g., Chien and Kim 2023). To compare to ACE2-ERA5 simulations, the 2001 to 2010 ERA5 and IMERG fields are regridded onto a 1-deg horizontal resolution, with 6-hourly output. For conciseness, we use "observations" to represent both the ERA5 reanalysis and IMERG satellite data throughout.

2.3 Detection of tropical cyclones

To detect tropical cyclones in ERA5 and ACE2-ERA5, we use the Tempest Extremes package (Ullrich and Zarzycki 2017) and largely follow the original Tempest Extremes paper, with some modest modifications. Tropical cyclone centers are detected where sea-level pressure is at a local minimum with a warm core aloft. In ERA5, the warm core is defined where geopotential heights between 300 and 500 hPa decrease by 58.8 m^2/s^2 within a 6.5 deg radial distance from the tropical cyclone center. Because the ACE2-ERA5 model does not provide geopotential height as an output, we use temperature at the third model level (T3) in the hybrid coordinate (corresponding to roughly 200-300 hPa) to detect the warm core in our simulations. Specifically, we require that T3 decrease by 0.4K over a 6.5 deg circle distance from the TC center in ACE2-ERA5, which is comparable to the geopotential criteria for ERA5. Note that the warm core criteria for ACE2-ERA5 follow those of Watt-Mayer et al. (2024).

After TC centers are identified, they are grouped together into the same TC case if the consecutive center locations are located within 8 deg of one another within a 6-hour window. In addition, to avoid false detection of TCs due to surface pressure corrections over land, we add criteria for (1) the surface elevation at the storm center being lower than 150 m for at least 60 hours and (2) the latitude of the TC center being occurring within 50°S-50°N for at least 60 hours.

Tropical cyclogenesis is defined as the first time that each TC case is detected. We only consider tropical cyclogenesis events that occur within 30°S-30°N to avoid the detection of extratropical-like cyclones, as in Fig. 2 in Ullrich and Zarzycki (2017).

2.4 Tropical cyclone genesis potential index (TCGI)

To validate if the ACE2-ERA5 physically represents TC genesis, the first step is to check if TC genesis occurs when and where the environmental conditions are favorable. Therefore, we investigate the relationship between TC genesis and the environment from subseasonal to interannual timescales. The environmental conditions are quantified by the genesis potential index, which represents how favorable the environmental conditions are for cyclogenesis. While various versions of this index have been developed over the decades to explain TC genesis on annual, interannual, and subseasonal timescales in observations and dynamical models (e.g., Emanuel and Nolan 2004; Carmargo et al. 2007ab; Tippett et al. 2011), they are qualitatively similar. Here, we specifically choose the genesis potential index (TCGI) defined in Tippett et al. (2011) because its input variables are more easily derived from the ACE2-ERA5 output and its coefficients are based on observations and reanalysis. The genesis potential index is defined as follows:

$$TCGI = \exp\,[\mathrm{b} + b_{\zeta} * \zeta + b_{RH} * RH + b_{SST} * SST + b_{\Lambda} * \Lambda + \ln(\cos(lat))]$$

, which considers vorticity at 850 hPa (ζ), column relative humidity (RH), vertical wind shear between 850hPa and 200 hPa (Λ), and sea surface temperature anomalies relative to the tropical mean averaged over 20°S-20°N (SST). The coefficients for each variable (b_x) are fitted from observation and reanalysis by Tippett et al. (2011). The coefficients are: b = -11.96, b_{ζ}= 1.12, b_{RH}= 0.12, b_{SST}= 0.46, and b_{Λ}= -0.13. The index is originally designed to explain the geographic distribution and seasonal cycle of TC genesis, where monthly mean variables are used. In this study, we diagnose monthly TCGI to explain the geographic distribution, seasonal cycle, and interannual variability of TC genesis. Further, we calculate instantaneous 6-hourly TCGI for subseasonal analysis: to evaluate how the environmental conditions vary with the Madden-Julian Oscillation.

2.5 Detection of Madden-Julian Oscillation (MJO) and convectively coupled equatorial waves (CCEWs)

2.5.1 Space-time decomposition of precipitation. We need to identify subseasonal variability (e.g., MJO and convectively coupled equatorial waves) to investigate environmental conditions that affect the subseasonal TC variation. We conduct a 2-dimensional space-time Fourier decomposition of precipitation anomalies (Wheeler and Kiladis 1999) to analyze the signal of MJO and convectively coupled equatorial waves (CCEWs). The anomalies are obtained by removing the time mean, the seasonal cycles, and the diurnal cycles. The seasonal cycle is computed as the first three harmonics of the daily annual cycle, and the diurnal cycle is computed by the average of each day from the entire simulations.

The space-time decomposition is a common diagnostic tool to understand tropical climate variability, originally developed by Wheeler and Kiladis (1999). The main idea is to decompose the space-time varying precipitation or convection signal into each zonal wavenumber and frequency component. By looking at the precipitation or cloud signals in wavenumber-frequency space, distinct modes of variabilities with unique propagation characteristics can be identified (e.g., MJO and each type of CCEWs). Here, we provide detailed descriptions of how the diagnostic is done. We first separate the precipitation anomalies into the symmetric and the antisymmetric components to the equator by averaging and subtracting precipitation anomalies in each hemisphere, respectively. We then meridionally average the symmetric and antisymmetric components separately. To increase statistical power, the meridionally averaged precipitation time series is separated into segments with a segment length of 96 days, with each segment overlapping for 60 days. Each segment is tapered by a Hanning window with a window length of 5 days and detrended. Afterward, we conduct space-time decomposition for each segment of the time series. We then average the space-time decomposition outcome of each segment to obtain the symmetric component of the raw power spectrum (Fig. S1a, d). The raw power spectrum presents strong signals in low-frequency components, which makes high-frequency components difficult to observe. The strong power in low-frequency components is due to the red noise of the atmosphere. To avoid the red noise dominating the spectrum, we normalize the raw spectrum by the background spectrum (Fig. S1c, f), obtained by apply 15 cycles of a centered 1-2-1 running mean over wavenumber space to average the raw symmetric and antisymmetric spectrum (Fig. S1b, e). The normalized spectrum shows the ratio (signal strength) of the raw power compared to the background noise. Here we show the normalized spectrum to identify MJO and CCEWs in Section 3.

2.5.2 Madden-Julian Oscillation index. The MJO signals are extracted using the RMM index, which was originally developed by Wheeler and Hendon (2004). The RMM index is obtained from the combined empirical orthogonal function (EOF) analysis of zonal wind anomalies at 850 hPa (U850) and 200 hPa (U200) and precipitation (PR) anomalies. Note that we use precipitation anomalies in this study instead of outgoing longwave radiation (OLR) because precipitation is a more common output variable for the AI models. Using precipitation to capture the MJO is common among dynamical

GCM studies (e.g., Ahn et al. 2017; 2020; Samarasinghe et al. 2021). The anomalies of U850, U200, and PR are obtained by removing the time mean and the seasonal and diurnal cycles mentioned in Section 2.3.1. In addition, these three fields are averaged meridionally between 15°S and 15°N, and the 120-day running mean is removed to reduce low-frequency variability. After obtaining the anomalies, we do the combined EOF analysis and find the most dominant structure in longitude. The two leading EOFs are obtained from observations, shown in Fig. S2. If the MJO signal in ACE2-ERA5 is pronounced, we expect a similar zonal structure of the MJO as in observations since ACE2-ERA5 is trained on ERA5 data. Therefore, the EOFs obtained from observations are also used as EOFs in ACE2-ERA5. The RMM1 and RMM2 indices are obtained by projecting the combined field of U850, U200, and PR anomalies onto the two leading EOFs. By diagnosing the RMM1 and RMM2 indices for each time, we then construct the 8-phase composite of the MJO (Fig. S3). The TC genesis and TCGI are then grouped with respect to each MJO phase.

3. Results

3.1 Mean state climate

We find that the mean state temperature, precipitation, and outgoing longwave radiation in ACE2-ERA5 are consistent with our understanding of the observed climatology, showing a clear Indo-Pacific warm pool (Fig. S4, left, upper), intertropical convection zone (ITCZ) (Fig. S4, left, middle), and low surface pressure in the tropics (Fig. S4, left, bottom). The global mean surface temperature, surface pressure, and precipitation are roughly conserved between 2001 and 2010 in our simulation (Fig. S4, right), although the global mean precipitation slightly increases, similar to what is described in Watt-Mayer et al. (2023; 2024). The stability of the simulation motivates us to further investigate tropical cyclogenesis in ACE2-ERA5.

3.2 Geographic distribution and seasonal cycle of TC genesis

Figure 1 shows the locations of TC genesis in ACE2-ERA5 (Simulation I) and ERA5 from 2001-2010. We find that, in general, TC genesis locations are well represented in the Northern Indian Ocean, Western Pacific, Eastern Pacific, North Atlantic, Southern Indian Ocean, and South Pacific. The number of TCs per year is 51 in ACE2-ERA5, which is comparable to 56 in ERA5 over the same ten-year period. The annual number of TCs in ACE2-ERA5 is closer to that of ERA5 compared to some high-resolution dynamical GCMs, which range from 10 to 120 TCs per year (e.g., Roberts et al. 2020). However, Figure 1 shows some underestimation of TCs in ACE2-ERA5 in coastal regions near India and Australia, in the South China Sea, and in the Eastern Pacific near Central America. We hypothesize that underestimation in coastal regions may be due to the lack of TC genesis events starting from local convection over land that propagate offshore (e.g.,Whitaker and Maloney 2020). These local processes could be difficult for AI models to capture. Note that there is also a slight underestimation of the number of TCs per year in ERA5 compared to Best Track (e.g., Schreck et al. 2014), and this discrepancy is partially explained by the fact that here we detect TCs using 1-deg ERA5 reanalysis instead of the native 0.25-deg resolution of ERA5. Our choice of using 1-deg ERA5 reanalysis is motivated by the need to compare as directly as possible to our ACE2-ERA5 simulation. We treat TCs in ERA5 as our baseline for the rest of this work.

The seasonal cycle of TC genesis in each basin is also well represented in ACE2-ERA5 compared to ERA5 (Fig. 2). Figure 2 shows that TC genesis number in each basin is similar to that of ERA5 observed in the North Western Pacific, North Eastern Pacific, and North Atlantic. In these basins, TC genesis events peak in the boreal summer months. Moreover, the ACE2-ERA5 model captures the rapid onset of TC season in the North Atlantic from July to September, as well as the more gradual increase of TC genesis between April and September in the North Western Pacific, consistent with findings in previous studies (e.g., Yang et al. 2021). In the Northern Indian Ocean, ACE2-ERA5 is also able to capture the two TC seasons in spring and autumn, although spring events are underestimated in ACE2-ERA5.

3.3 Geographic distribution and seasonal cycle of TCGI

To understand whether TC genesis occurs with favorable environmental conditions in ACE2-ERA5, we analyze the genesis potential index (TCGI). The TCGI map is shown in Figure 3, showing hotspots in the North Western Pacific, along the ITCZ, South Western Pacific, and the South Indian Ocean in ERA5, consistent with previous studies (Fig. 3 in Tippett et al. 2011). In ACE2-ERA5, we find that the magnitude of TCGI is larger than that of ERA5. This is largely due to the weaker vertical wind shear in ACE2-ERA5 (Fig. S5) since the vorticity and column relative humidity are similar between the two datasets (Fig. S6-7), and the sea surface temperature is identical by design (Fig. S8). The pattern of TCGI in ACE2-ERA5 also shows hotspots in the Indian Ocean, Western Pacific, Eastern Pacific ITCZ, and Atlantic ITCZ, although TCGI hotspots in ACE2-ERA5 are closer to the equator than those in ERA5 due to smaller vertical wind shear near the equator. We speculate that the smaller vertical wind shear near the equator is due to weaker CCEWs (more details in Section 3.4). Overall, we find that TC genesis generally occurs at locations where TCGI is high in both ERA5 and ACE2-ERA5.

The seasonal cycle of TCGI in ERA5 (Fig. 4, top) generally shows a single peak in summer seasons (between May and October in the northern hemisphere and between November and April in the southern hemisphere) in most basins and two peaks in the North Indian Ocean, consistent with TC genesis in ERA5. TC genesis and TCGI are the best aligned with each other in the North Western Pacific and North Eastern Pacific. However, in the North Atlantic, TCGI gradually increases from April to August, while TC genesis increases rapidly between July and September. In addition to TCGI, the rapid onset of TC genesis is also because tropical cyclone seeds (i.e., precursor disturbances) are more abundant after July in the North Atlantic (Yang et al., 2021). In ACE2-ERA5, it is also the case that the TCGI increases gradually in the North Atlantic (Fig. 4, bottom), while the actual number of TC genesis events increases more rapidly.

Figure 5 further illustrates the relationship between TC genesis and the large-scale environment by showing the 2-dimensional histogram of TC genesis and TCGI for each month for each year in both ERA5 and ACE2-ERA5. Except for the North Indian Ocean, TC genesis and TCGI are positively correlated with correlation coefficients ranging from 0.6 to 0.7 in ERA5 and 0.5 to 0.7 in ACE2-ERA5.

3.4 Interannual variability of TC genesis and TCGI

Both internal atmospheric variability and external forcings (e.g., SST and greenhouse gas) affect TC genesis. That is, for the same SST and greenhouse gas forcings, the number of TC genesis per year could vary due to internal atmospheric variability, and that observations only represent one realization under given external forcings. To consider both internal and external effects on TC genesis, we use 10 ensemble members of ACE2-ERA5 simulations (Simulation II) instead of a single member (Simulation I) to investigate the interannual variability of TC genesis and TCGI. Considering all 10 ensemble members (Fig. 6, light blue shading), the ERA5 observations (Fig, 6, black line) lie within the ACE2-ERA5 ensemble spread in most basins. The trend of the ACE2-ERA5 ensemble mean (Fig. 6, blue line) likely represents the effect of external forcings (which includes SSTs) on TC genesis, while the ensemble spread represents the internal variability. When the observed TC genesis trend aligns with the trend of the ensemble mean, it suggests that this trend is likely due to external forcings as opposed to internal variability. For example, the observations and the ensemble mean of ACE2-ERA5 both show a decrease in the North Western Pacific between 2001 and 2010 and an increase in TC genesis in 2009 in the North Eastern Pacific (likely due to the 2009 El Nino). ACE2-ERA5 underestimates TC genesis in the Indian Ocean in ACE2-ERA5 due to the lack of coastal TC genesis mentioned in Section 3.2. Because of this, the spread between 10 ensemble members does not fully cover the observed TC annual number (Fig. S9). We focus on the major TC basins, including the North Atlantic, North Western Pacific, and North Eastern Pacific, in the remainder of this section.

To further investigate if the interannual relationship between environmental conditions and TC genesis match between ACE2-ERA5 and ERA5, we examine the annually-averaged TC genesis count and TCGI in Fig. 7. We find that TC number and TC genesis index are positively correlated in both ERA5 and ACE2-ERA5, with the highest correlation in North Atlantic (Fig. 7a, d) and slightly lower in North Western Pacific and North Eastern Pacific (Fig. 7b, c, e, f). The correlation coefficient is between 0.14 to 0.38 in ERA5 and 0.12 to 0.25 in ACE2-ERA5. Note that the other basins have a low correlation between TC genesis and TCGI, likely due to other factors (e.g., number of TC seed disturbances) regulating TC genesis variability. Compared to the correlation between TC genesis and the environment on monthly time scales (Fig. 5), the correlation on interannual time scales is lower, suggesting that the variability of precursor disturbance could play a significant role in regulating TC frequency (e.g., Ikehata and Satoh 2021). We do not explore this further.

3.5 Subseasonal variability of TC genesis and TCGI

This section sequentially examines (1) how MJO and CCEWs are represented in ACE2-ERA5, (2) MJO propagation and its 3D structure, and (3) the modulation of TC genesis by the MJO.

3.5.1 Subseasonal variabilities of precipitation

To analyze the signal of MJO and convectively coupled equatorial waves (CCEWs), we show the normalized spectrum of precipitation anomalies (i.e., the signal strength, the ratio of the raw spectrum relative to the background spectrum) in shading in Fig. 8. For the eastward propagation regime, between zonal wavenumber 1-5 and period 30-90 days, the MJO signal in ACE2-ERA5 (red box) is pronounced. The signal strength of the MJO in ACE2-ERA5 is comparable to that in satellite observations.

Gray lines on top of the normalized power spectrum are the theoretical dispersion curves for each type of CCEW from Matsuno (1966). For the eastward propagating regime with higher frequencies and smaller spatial scales (periods of 2.5 to 20 days and zonal wavenumbers 1-15), the convectively coupled Kelvin waves (KWs) (blue polygon) are significant. The highest signal strength of KWs aligns with the slanted dispersion lines, which represent equivalent depths between 8 and 90 m.

For the westward propagating regime, the lower frequency equatorial Rossby waves (green shape) are also pronounced in

ACE2-ERA5, although the signals have two peaks in zonal wavenumbers (zonal wavenumber 4 and 7-10 in ACE2) while in observations, there is only one maximum cantered around zonal wavenumbers 1 to 5. For the higher-frequency regime of westward-propagating disturbances s (periods between 3 to 10 days), tropical-depression-type (TD-type) variability is weaker compared to the observations. For even higher frequencies (periods shorter than 3 days), the westward-propagating inertial gravity waves (WIG) are much weaker in ACE2-ERA5 than in observations. In the antisymmetric spectrum (Fig. S9), the westward-propagating mixed Rossby gravity (MRG) waves are also pronounced in ACE2-ERA5.

Overall, in ACE2-ERA5, the low-frequency variability (convectively coupled Kelvin waves, equatorial Rossby waves, and the MJO) are more comparable to observations, while the high-frequency variabilities (TD-type variability and westward-propagating inertial gravity waves) are underestimated.

Previous studies have shown that the MJO and convectively coupled equatorial waves can modulate TC genesis, with the MJO-TC relationship being the most extensively documented (e.g., Maloney and Hartmann, 2000; Carmargo et al., 2009). We next examine how well ACE2-ERA5 captures the MJO modulation of TCs to validate whether ACE2-ERA5 captures the subseasonal variability of TC genesis and the environment.

3.5.2 MJO modulation of TC genesis

The evolution of MJO propagation of precipitation is similar to observed, although the magnitude is slightly weaker in ACE2-ERA5 (Fig. S10). As in observations, the ACE2-ERA5 simulation can represent the MJO precipitation after crossing the Maritime continent (e.g., Zhang and Ling 2017) with the consistent eastward propagation of zonal wind anomalies at 850 hPa and 200 hPa (Fig. S11). This suggests that the ACE2-ERA5 model is able to capture the three-dimensional structure of the MJO with realistic propagation.

Given the realism of the MJO in ACE2-ERA5, we investigate how TC genesis counts and TCGI vary as a function of the MJO phase in boreal summer (May to October) (Figure 9). Figure 9 shows that positive TCGI anomalies propagate eastward following the enhanced envelope of the MJO, with a similar northwest-southeast tilt. The eastward propagation of TCGI anomalies as the MJO evolves is qualitatively similar between observations and ACE2-ERA5, except that the magnitude of TCGI anomalies in ACE2-ERA5 is higher than that in observations. Furthermore, the locations and timings of positive TCGI anomalies correspond to an increase in TC genesis events (shown in dots in Fig. 9) in both observations and ACE2-ERA5. For example, during MJO phases 5-7 when precipitation is enhanced in the western Pacific (green box), positive TCGI anomalies result in more TC genesis events. During MJO phases 3-4 when precipitation is suppressed in the western Pacific, negative TCGI anomalies result in fewer TC genesis events. TC genesis and TCGI in the western Pacific are positively correlated in ACE2-ERA5 as in observations (Fig. 11a, c) and previous studies (e.g., Fowler and Pritchard 2020; Emlaw and Kim 2024).

Figure 10 shows that during the austral summer (November to April) in ACE2-ERA5, the geographic distribution of TCGI anomalies and TC genesis events associated with the MJO also resembles that in observations. TCGI follows the enhanced convection envelope of the MJO into the Southern Hemisphere, with a clearer east-west elongated shape. In Phases 3 and 4, TCGI enhances over the Southern Indian Ocean near the Maritime continent and promotes more TC genesis events. As the MJO envelope propagates eastward in Phases 7 and 8, TCGI enhances in the South Pacific and favors more TC genesis in that region. Figure 11b, d clearly shows the alignment of maximum TC genesis and positive TCGI in ACE2-ERA5 and observations, especially in phase 7.

The ACE2-ERA5 simulation is able to capture the eastward propagation of the MJO's modulation of TC genesis, as well as the seasonal shifts of this signal into the Northern or Southern Hemisphere. Note that we chose a smaller domain in Fig. 11 to better capture the local features of the MJO, instead of the larger domain of the North Western Pacific and Southern Pacific in Fig. 1. However, Figure S12 shows that the MJO modulation of TC genesis using the large domain in Fig. 1 is qualitatively consistent with the results in Fig. 11. While we only show the Western Pacific and Southern Pacific in Fig. 11, similar conclusions can be found in other basins in Fig. S12-13. In particular, although MJO convection is weaker crossing the dateline, the MJO could also affect TC genesis in the Atlantic Ocean, likely through the modulation of vertical wind shear and vorticity by the MJO circulation (Fig. S11, Phase 6-8 in upper panel, Zhao and Li 2019). We find that the MJO's effect on Atlantic TC genesis in ACE2-ERA5 is also qualitatively similar to the observations (Fig. S12, d.1-d.2), suggesting that ACE2-ERA5 can capture both the convection and the circulation of the MJO over the globe.

4. Conclusions and implications

This study thoroughly examines tropical cyclone (TC) genesis and its modulation by the environment on interannual, annual, and subseasonal timescales using the Ai2 Climate Emulator version 2 (ACE2) deep-learning model. The geographical distribution and seasonal cycle of TC genesis in each basin are generally well represented in ACE2-ERA5, although some underestimation is found near coastal regions. We conduct 10 ensemble-member experiments using ACE2-ERA5 to capture the variability of TC genesis due to both the external forcings (SST and greenhouse gases) and internal atmospheric variability. The interannual variability of TC genesis numbers varies significantly across ensemble members, highlighting the variability of TC numbers for a given forcing for each year. Regardless, the observed annual TC number falls within the ACE-ERA5 ensemble. In general, TC genesis in ACE2-ERA5 tends to occur when and where the environmental conditions are favorable (high genesis potential index, TCGI) on interannual, annual, and subseasonal timescales, although the correlation is slightly lower than observations in some circumstances.

On subseasonal timescales, the precipitation signal strength of convectively coupled Kelvin waves (KWs), equatorial Rossby waves (ERs), and the Madden-Julian Oscillation (MJO) in ACE2-ERA5 are comparable to observations. Further, the temporal and spatial scales of the waves, as well as their dispersion relationships, also resemble those observed. The representation of convectively coupled equatorial waves and MJO in ACE2-ERA5 is more realistic than many global climate models (GCMs) in Coupled Model Intercomparison Project phase 6 (CMIP6) (Fig. S14; Bartana et al. 2023). The MJO eastward propagation is pronounced in ACE2-ERA5, with a 3-dimensional circulation structure consistent with precipitation. The modulation of TC genesis and TCGI by the MJO is also reasonably represented in ACE2-ERA5.

The results of this study demonstrate great promise for the use of AI emulators for climate science research. For example, the consistent relationship between TC genesis and the environment in ACE2-ERA5 on various timescales suggests that it may be feasible to investigate the sensitivity of TC genesis under varying SSTs, as we do in dynamical GCMs (e.g., Bacmeister et al. 2018). In addition, ACE2-ERA5 representation of subseasonal variability suggests that it may be adequate for probing fundamental questions about convectively coupled equatorial waves, the MJO, and mechanisms by which they modulate TC genesis (e.g., Kim et al. 2011; Chien and Kim 2024; Rios-Berrios et al. 2024). Furthermore, although this study focused on the present-day climate, the positive correlation between annual TC number and annual TCGI anomalies suggests that it may be possible to use these data-driven models to investigate TC genesis under different SSTs and greenhouse gas scenarios mimicking past or future climates. However, because those scenarios fall outside the training period, to what extent data-driven climate models can extrapolate what they have learned to unseen climate states requires additional study (see also Watt-Mayer et al. 2024).

Tropical cyclogenesis and tropical waves are historically difficult to represent well in dynamical GCMs because they require an accurate representation of subgrid-scale convection and its effect on the grid-scale variables. Convective parameterizations are primary sources of discrepancies among GCMs in simulating processes related to tropical convection (e.g., Straub et al. 2010; Lee et al. 2025). Different from the dynamical GCMs that highly rely on parameterizing the sub-grid scale processes correctly to simulate large-scale variabilities, these AI emulators learn relationships between the large-scale environment and TC genesis (or tropical waves) without explicitly representing the small-scale convective processes. We believe that this is one reason that ACE2-ERA5 can represent TC genesis and tropical waves with fidelity at a 1-degree resolution. The ability to run simulations at comparatively low resolutions but still capture the effects of small-scale processes remains one of the most exciting innovations of AI emulators.

While we only use a single AI model, whether other AI models also capture the correlation between large-scale environments and small-scale phenomena must still be verified, as different model architectures and training procedures can lead to significantly different results (e.g., Pathak et al. 2022; Kurth et al. 2023). Although the overall environmental modulation of TC genesis from subseasonal-to-interannual timescales in ACE2-ERA5 resembles the observed, we acknowledge some limitations in this model. For example, there is a slight underestimation of coastal TC genesis, weaker high-frequency tropical variability (TD-wave and inertial gravity wave), and a larger magnitude of TCGI. Exactly why those model deficiencies occur requires further investigation. Lastly, this study does not consider tropical cyclone seed disturbances but only focuses on the effect of environmental conditions on TC genesis. Future studies can examine how the variability of TC seed disturbances affects TC genesis in AI emulators.

Acknowledgements

We acknowledge code sharing from Jihong Moon on tropical cyclone tracking and Yi Xia on TCGI calculation. This work was funded, in part, by the Heising-Simons Foundation grant #2023-4720. EDM was funded by NOAA CVP grant NA22OAR4310609 and NSF grant AGS-2217785.

Data availability statements

The analysis code and data used in this study are publicly available on GitHub (https://github.com/muting-chien/TC_genesis_ACE2_evaluation_public/) and will be posted on Zenodo with a DOI before publication.

References

Ahn, M.S., Kim, D., Sperber, K.R., Kang, I.S., Maloney, E., Waliser, D., Hendon, H. and WGNE MJO Task Force, 2017. MJO simulation in CMIP5 climate models: MJO skill metrics and process-oriented diagnosis. *Climate Dynamics*, *49*, pp.4023-4045.

Ahn, M.S., Kim, D., Kang, D., Lee, J., Sperber, K.R., Gleckler, P.J., Jiang, X., Ham, Y.G. and Kim, H., 2020. MJO propagation across the Maritime Continent: Are CMIP6 models better than CMIP5 models?. *Geophysical Research Letters*, *47*(11), p.e2020GL087250.

Bi, K., Xie, L., Zhang, H., Chen, X., Gu, X. and Tian, Q., 2022. Pangu-weather: A 3d high-resolution model for fast and accurate global weather forecast. *arXiv preprint arXiv:2211.02556*.

Bacmeister, J.T., Reed, K.A., Hannay, C., Lawrence, P., Bates, S., Truesdale, J.E., Rosenbloom, N. and Levy, M., 2018. Projected changes in tropical cyclone activity under future warming scenarios using a high-resolution climate model. Climatic Change, 146(3), pp.547-560.

Bartana, H., Garfinkel, C.I., Shamir, O. and Rao, J., 2023. Projected future changes in equatorial wave spectrum in CMIP6. *Climate Dynamics*, *60*(11), pp.3277-3289.

Bi, K., Xie, L., Zhang, H., Chen, X., Gu, X., & Tian, Q. (2022). Pangu-weather: A 3d high-resolution model for fast and accurate global weather forecast. *arXiv preprint arXiv:2211.02556*.

Bi, K., Xie, L., Zhang, H., Chen, X., Gu, X. and Tian, Q., 2023. Accurate medium-range global weather forecasting with 3D neural networks. *Nature*, *619*(7970), pp.533-538.

Bonavita, M., 2024. On some limitations of current machine learning weather prediction models. *Geophysical Research Letters*, *51*(12), p.e2023GL107377.

Bonev, B., Kurth, T., Hundt, C., Pathak, J., Baust, M., Kashinath, K. and Anandkumar, A., 2023, July. Spherical fourier neural operators: Learning stable dynamics on the sphere. In *International conference on machine learning* (pp. 2806-2823). PMLR.

Camargo, S.J., Emanuel, K.A. and Sobel, A.H., 2007a. Use of a genesis potential index to diagnose ENSO effects on tropical cyclone genesis. *Journal of Climate*, *20*(19), pp.4819-4834.

Camargo, S., Sobel, A.H., Barnston, A.G. and Emanuel, K.A., 2007b. Tropical cyclone genesis potential index in climate models. *Tellus A: Dynamic Meteorology and Oceanography*, *59*(4), pp.428-443.

Camargo, S.J., Wheeler, M.C. and Sobel, A.H., 2009. Diagnosis of the MJO modulation of tropical cyclogenesis using an empirical index. *Journal of the Atmospheric Sciences*, *66*(10), pp.3061-3074.

Chien, M.T. and Kim, D., 2023. Representation of the convectively coupled Kelvin waves in modern reanalysis products. *Journal of the Atmospheric Sciences, 80(2)*, pp.397-418.

Chien, M.T. and Kim, D., 2024. Response of convectively coupled Kelvin waves to surface temperature forcing in aquaplanet simulations. *Journal of Advances in Modeling Earth Systems, 16(10)*, p.e2024MS004378.

Cresswell-Clay, N., Liu, B., Durran, D., Liu, A., Espinosa, Z.I., Moreno, R. and Karlbauer, M., 2024. A deep learning earth system model for stable and efficient simulation of the current climate. *arXiv preprint arXiv:2409.16247*.

DeMaria, M., Franklin, J.L., Chirokova, G., Radford, J., DeMaria, R., Musgrave, K.D. and Ebert-Uphoff, I., 2024. Evaluation of Tropical Cyclone Track and Intensity Forecasts from Artificial Intelligence Weather Prediction (AIWP) Models. *arXiv preprint arXiv:2409.06735*.

Emanuel, K.A. and Nolan, D.S., 2004, May. Tropical cyclone activity and the global climate system. In *26th Conf. on Hurricanes and Tropical Meteorology* (pp. 240-241).

Emlaw, G.N. and Kim, D., 2024. The role of precursor disturbances on the modulation of western Pacific tropical cyclogenesis by the Madden-Julian oscillation. *Geophysical Research Letters*, *51*(12), p.e2023GL108102.

Feng, X., Yang, G.Y., Hodges, K.I. and Methven, J., 2023. Equatorial waves as useful precursors to tropical cyclone occurrence and intensification. *Nature Communications*, *14*(1), p.511.

Fowler, M.D. and Pritchard, M.S., 2020. Regional MJO modulation of Northwest Pacific tropical cyclones driven by multiple transient controls. *Geophysical Research Letters*, *47*(11), p.e2020GL087148.

Gray, W.M., 1975. Tropical cyclone genesis.

Hersbach, H., Bell, B., Berrisford, P., Hirahara, S., Horányi, A., Muñoz-Sabater, J., Nicolas, J., Peubey, C., Radu, R., Schepers, D. and Simmons, A., 2020. The ERA5 global reanalysis. *Quarterly journal of the royal meteorological society*, *146*(730), pp.1999-2049.

Huffman, G.J., Bolvin, D.T., Braithwaite, D., Hsu, K.L., Joyce, R.J., Kidd, C., Nelkin, E.J., Sorooshian, S., Stocker, E.F., Tan, J. and Wolff, D.B., 2020. Integrated multi-satellite retrievals for the global precipitation measurement (GPM) mission (IMERG). *Satellite precipitation measurement: Volume 1*, pp.343-353.

Ikehata, K., & Satoh, M. (2021). Climatology of tropical cyclone seed frequency and survival rate in tropical cyclones. *Geophysical Research Letters*, *48*(18), e2021GL093626.

Kim, D., Sobel, A.H. and Kang, I.S., 2011. A mechanism denial study on the Madden-Julian Oscillation. *Journal of Advances in Modeling Earth Systems, 3(4).*

Kurth, T., Subramanian, S., Harrington, P., Pathak, J., Mardani, M., Hall, D., Miele, A., Kashinath, K. and Anandkumar, A., 2023, June. Fourcastnet: Accelerating global high-resolution weather forecasting using adaptive fourier neural operators. *In Proceedings of the platform for advanced scientific computing conference (pp. 1-11).*

Lam, R., Sanchez-Gonzalez, A., Willson, M., Wirnsberger, P., Fortunato, M., Alet, F., Ravuri, S., Ewalds, T., Eaton-Rosen, Z., Hu,

W. and Merose, A., 2023. Learning skillful medium-range global weather forecasting. *Science*, *382*(6677), pp.1416-1421.

Lee, S.-H., Park, S.-H., Chien, M.-T., & Kim, D. (2025). Simulations of Convectively Coupled Kelvin Waves (CCKWs) with Three Different Cumulus Parameterization Schemes. *Journal of Geophysical Research – Atmosphere*, accepted.

Maloney, E.D. and Hartmann, D.L., 2000. Modulation of eastern North Pacific hurricanes by the Madden–Julian oscillation. *Journal of climate*, *13*(9), pp.1451-1460.

Pathak, J., Subramanian, S., Harrington, P., Raja, S., Chattopadhyay, A., Mardani, M., ... & Anandkumar, A. (2022). Fourcastnet: A global data-driven high-resolution weather model using adaptive fourier neural operators. *arXiv preprint arXiv:2202.11214*.

Rios-Berrios, R., Tang, B.H., Davis, C.A. and Martinez, J., 2024. Modulation of tropical cyclogenesis by convectively coupled Kelvin waves. *Monthly Weather Review*, *152*(10), pp.2309-2322.

Roberts, M.J., Camp, J., Seddon, J., Vidale, P.L., Hodges, K., Vannière, B., Mecking, J., Haarsma, R., Bellucci, A., Scoccimarro, E. and Caron, L.P., 2020. Projected future changes in tropical cyclones using the CMIP6 HighResMIP multimodel ensemble. *Geophysical research letters*, *47*(14), p.e2020GL088662.

Samarasinghe, S.M., Connolly, C., Barnes, E.A., Ebert-Uphoff, I. and Sun, L., 2021. Strengthened causal connections between the MJO and the North Atlantic with climate warming. *Geophysical Research Letters*, *48*(5), p.e2020GL091168.

Schreck III, C.J., Molinari, J. and Aiyyer, A., 2012. A global view of equatorial waves and tropical cyclogenesis. *Monthly Weather Review*, *140*(3), pp.774-788.

Schreck III, C. J., Knapp, K. R., & Kossin, J. P. (2014). The impact of best track discrepancies on global tropical cyclone climatologies using IBTrACS. *Monthly Weather Review*, *142*(10), 3881-3899.

Sobel, A.H., Wing, A.A., Camargo, S.J., Patricola, C.M., Vecchi, G.A., Lee, C.Y. and Tippett, M.K., 2021. Tropical cyclone frequency. *Earth's Future, 9(12)*, p.e2021EF002275.

Straub, K. H., Haertel, P. T., & Kiladis, G. N. (2010). An Analysis of Convectively Coupled Kelvin Waves in 20 WCRP CMIP3 Global Coupled Climate Models. *Journal of Climate, 23(11)*, 3031–3056.

Tippett, M.K., Camargo, S.J. and Sobel, A.H., 2011. A Poisson regression index for tropical cyclone genesis and the role of large-scale vorticity in genesis. *Journal of Climate*, *24*(9), pp.2335-2357.

Ullrich, P.A. and Zarzycki, C.M., 2017. TempestExtremes: A framework for scale-insensitive pointwise feature tracking on unstructured grids. *Geoscientific Model Development*, *10*(3), pp.1069-1090.

Watt-Meyer, O., Dresdner, G., McGibbon, J., Clark, S.K., Henn, B., Duncan, J., Brenowitz, N.D., Kashinath, K., Pritchard, M.S., Bonev, B. and Peters, M.E., 2023. ACE: A fast, skillful learned global atmospheric model for climate prediction. *arXiv preprint arXiv:2310.02074*.

Watt-Meyer, O., Henn, B., McGibbon, J., Clark, S.K., Kwa, A., Perkins, W.A., Wu, E., Harris, L. and Bretherton, C.S., 2024. ACE2: Accurately learning subseasonal to decadal atmospheric variability and forced responses. *arXiv preprint arXiv:2411.11268*.

Weyn, J.A., Durran, D.R. and Caruana, R., 2019. Can machines learn to predict weather? Using deep learning to predict gridded 500-hPa geopotential height from historical weather data. *Journal of Advances in Modeling Earth Systems*, *11*(8), pp.2680-2693.

Weyn, J.A., Durran, D.R., Caruana, R. and Cresswell-Clay, N., 2021. Sub-seasonal forecasting with a large ensemble of deep-learning weather prediction models. *Journal of Advances in Modeling Earth Systems*, *13*(7), p.e2021MS002502.

Wheeler, M. and Kiladis, G.N., 1999. Convectively coupled equatorial waves: Analysis of clouds and temperature in the wavenumber–frequency domain. *Journal of the Atmospheric Sciences*, *56*(3), pp.374-399.

Wheeler, M.C. and Hendon, H.H., 2004. An all-season real-time multivariate MJO index: Development of an index for monitoring and prediction. *Monthly weather review*, *132*(8), pp.1917-1932.

Whitaker, J. W., & Maloney, E. D. (2020). Genesis of an east Pacific easterly wave from a Panama Bight MCS: A case study analysis from June 2012. *Journal of the Atmospheric Sciences*, *77*(10), 3567-3584.

Wu, L. and Takahashi, M., 2018. Contributions of tropical waves to tropical cyclone genesis over the western North Pacific. *Climate Dynamics*, *50*, pp.4635-4649.

Yamada, Y., Kodama, C., Satoh, M., Sugi, M., Roberts, M.J., Mizuta, R., Noda, A.T., Nasuno, T., Nakano, M. and Vidale, P.L., 2021. Evaluation of the contribution of tropical cyclone seeds to changes in tropical cyclone frequency due to global warming in high-resolution multi-model ensemble simulations. *Progress in Earth and Planetary Science*, *8*, pp.1-17.

Yang, W., Hsieh, T.L. and Vecchi, G.A., 2021. Hurricane annual cycle controlled by both seeds and genesis probability. *Proceedings of the National Academy of Sciences*, *118*(41), p.e2108397118.

Yoshida, K., Sugi, M., Mizuta, R., Murakami, H. and Ishii, M., 2017. Future changes in tropical cyclone activity in high-resolution large-ensemble simulations. *Geophysical Research Letters*, *44*(19), pp.9910-9917.

Zhao, C. and Li, T., 2019. Basin dependence of the MJO modulating tropical cyclone genesis. *Climate Dynamics*, 52(9), pp.6081-6096.

Zhang, C., & Ling, J. (2017). Barrier effect of the Indo-Pacific Maritime Continent on the MJO: Perspectives from tracking MJO precipitation. *Journal of Climate*, *30*(9), 3439-3459.

IOP Publishing
Machine Learning: Earth
Journal **XX** (XXXX) XXXXXX
https://doi.org/XXXX/XXXX

Figures

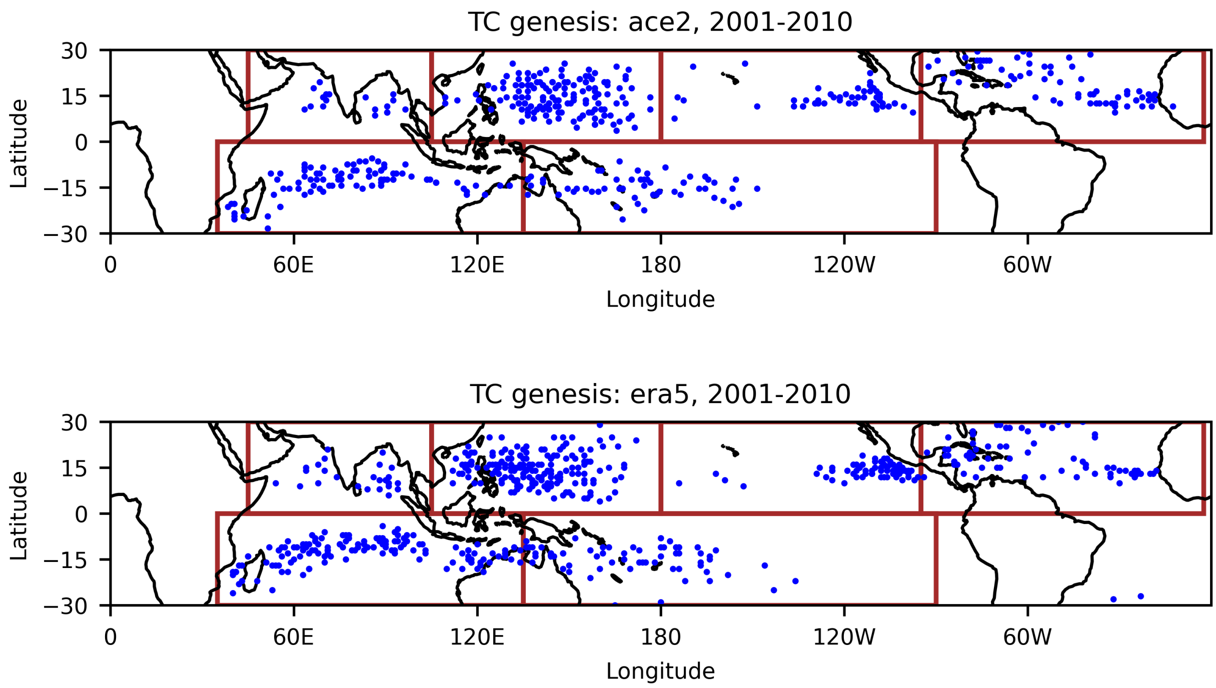

Figure 1. Map of TC genesis between 2001 and 2010 in (top) ACE2 (simulation I) and (bottom) ERA5. The brown boxes indicate each basin. In the northern hemisphere, the boxes from left to right represent the North Indian Ocean, North Western Pacific, North Eastern Pacific, and North Atlantic basin. In the southern hemisphere, the boxes from left to right represent the Southern Indian Ocean and the Southern Pacific Ocean.

IOP Publishing Machine Learning: Earth
Journal **XX** (XXXX) XXXXXX https://doi.org/XXXX/XXXX

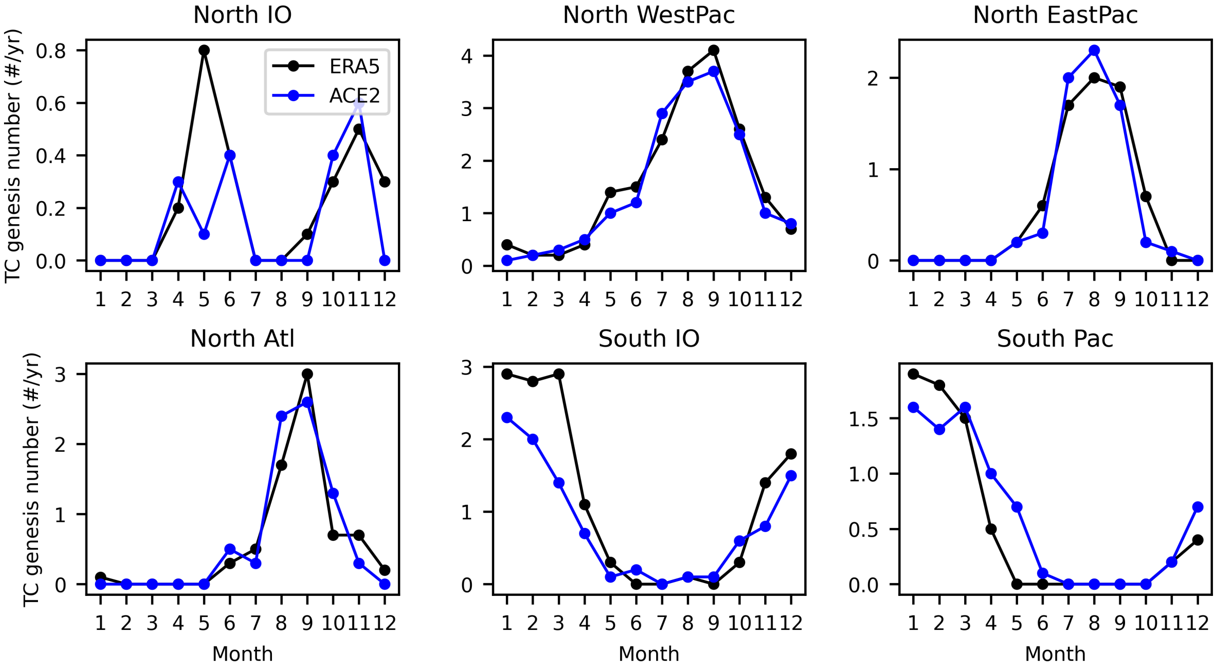

Figure 2. Seasonal cycle of TC genesis in each ocean basin. Black lines represent ERA5 and blue lines represent ACE2 (simulation I).

IOP Publishing
Machine Learning: Earth
Journal **XX** (XXXX) XXXXXX
https://doi.org/XXXX/XXXX

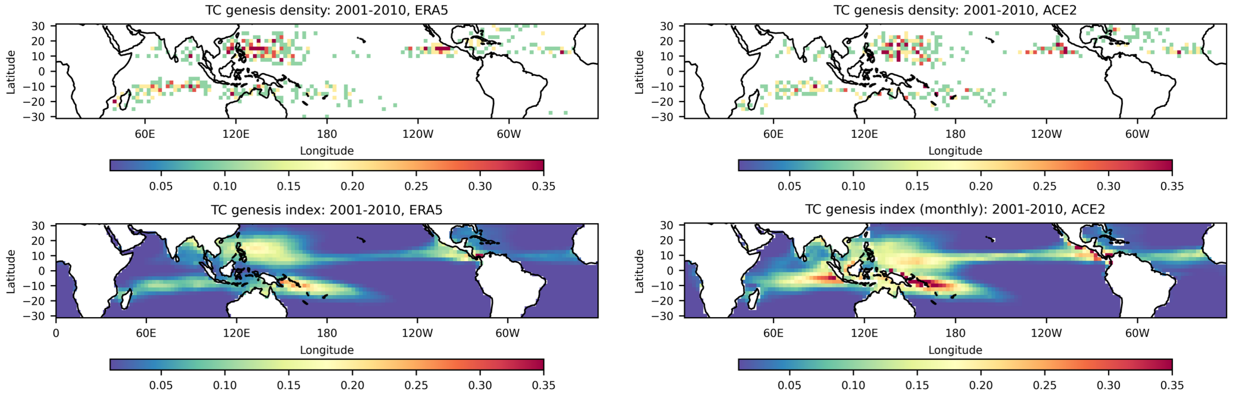

Figure 3. Top panel: TC genesis density. Bottom panel: TC genesis index. Left: ERA5, Right: ACE2 (simulation I)

IOP Publishing Machine Learning: Earth
Journal **XX** (XXXX) XXXXXX https://doi.org/XXXX/XXXX

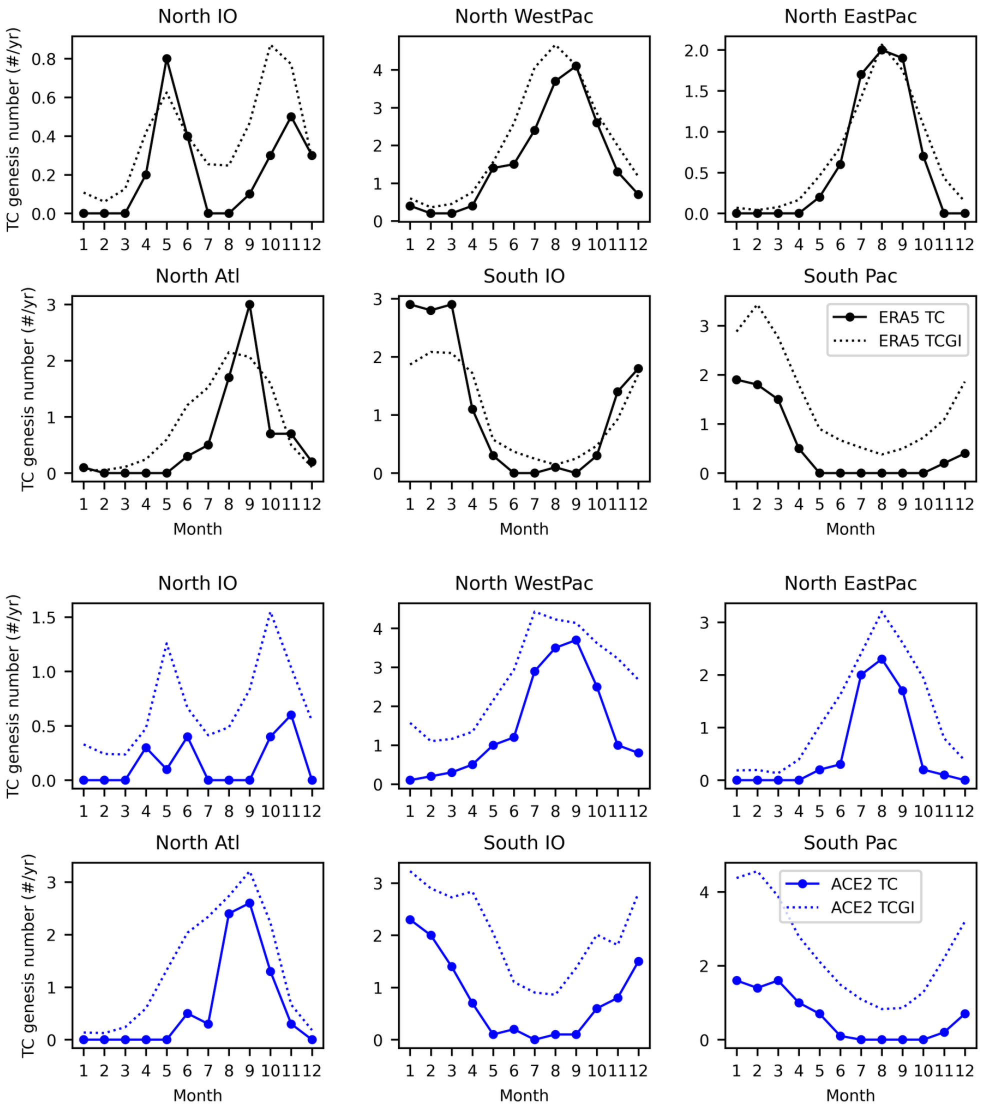

Figure 4. Seasonal cycle of TC genesis and TCGI in each basin in ERA5 (top) and ACE2 (Simulation I) (bottom).

IOP Publishing Machine Learning: Earth
Journal XX (XXXX) XXXXXX https://doi.org/XXXX/XXXX

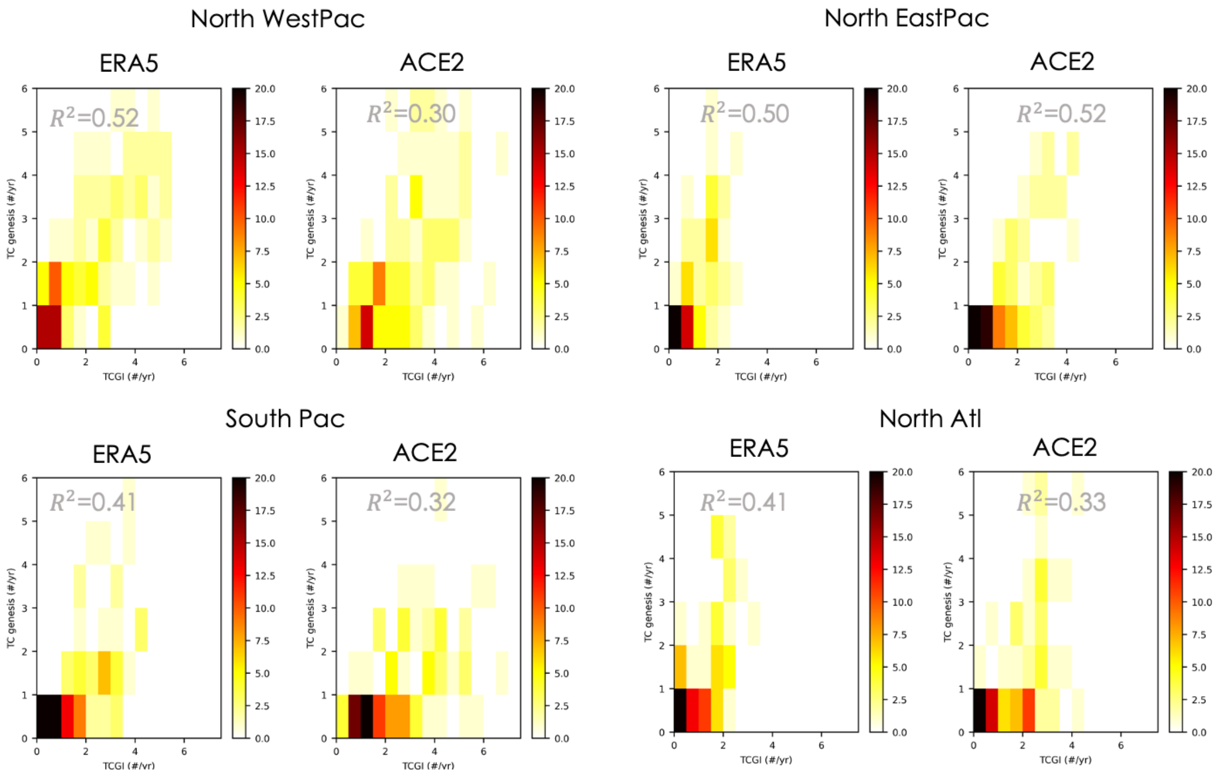

Figure 5. 2-D histograms of TC genesis and TCGI for each month for each year in ERA5 and ACE2 (Simulation I) in North Western Pacific (top left), North Eastern Pacific (top right), Southern Pacific (bottom left), and North Atlantic (bottom right).

IOP Publishing Machine Learning: Earth
Journal **XX** (XXXX) XXXXXX https://doi.org/XXXX/XXXX

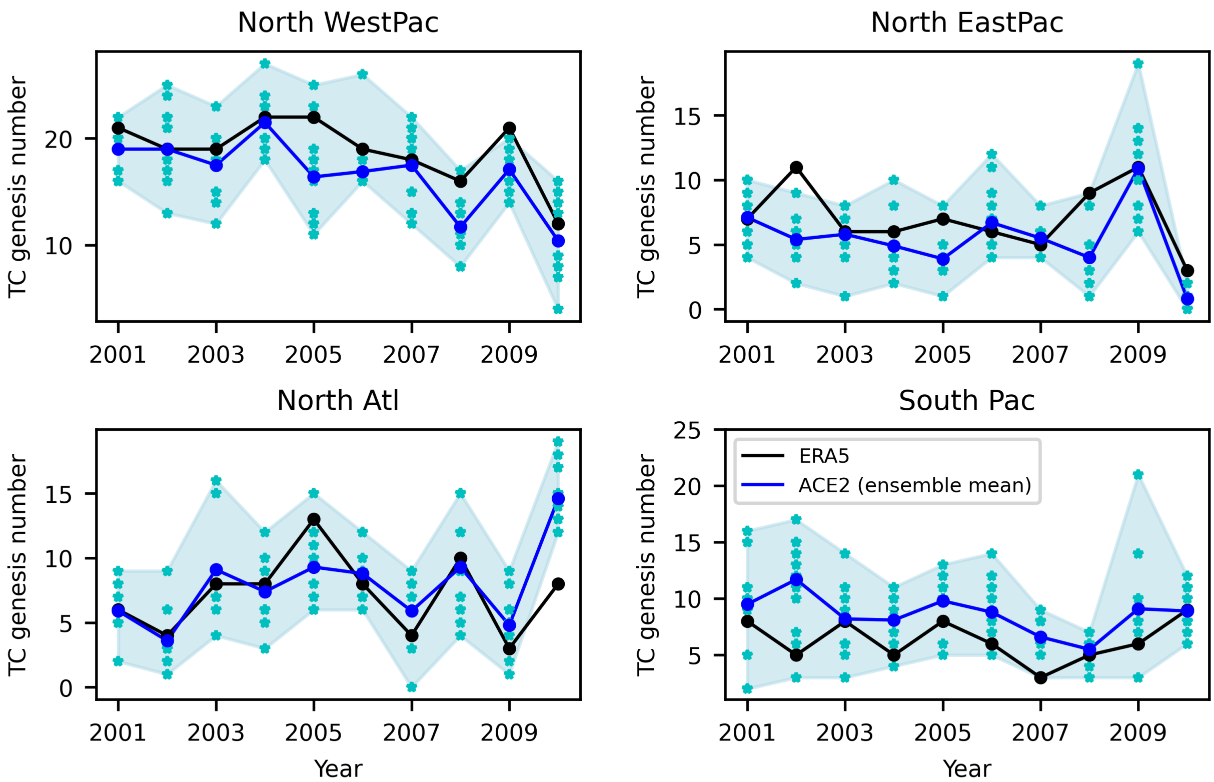

Figure 6. Interannual variability of TC genesis in ERA5 (black line), ACE2 (ensemble mean of Simulation II, dark blue line), and 10 members from ACE2 (Simulation II, light blue stars). Shading represents the ensemble spread.

IOP Publishing
Machine Learning: Earth
Journal **XX** (XXXX) XXXXXX
https://doi.org/XXXX/XXXX

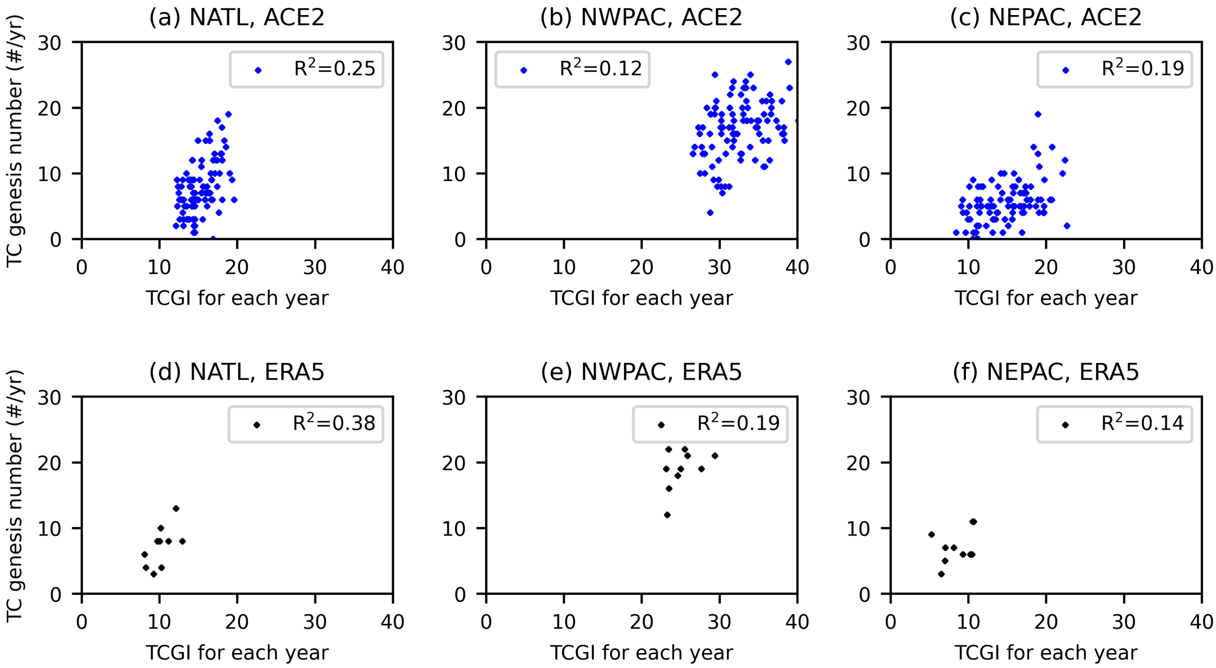

Figure 7. Interannual variability of TC genesis and TCGI in (a-c) ACE2 (Simulation II) and (d-f) ERA5. (a, d) North Atlantic, (b, e) North Western Pacific, and (c, f) North Eastern Pacific.

IOP Publishing Machine Learning: Earth
Journal **XX** (XXXX) XXXXXX https://doi.org/XXXX/XXXX

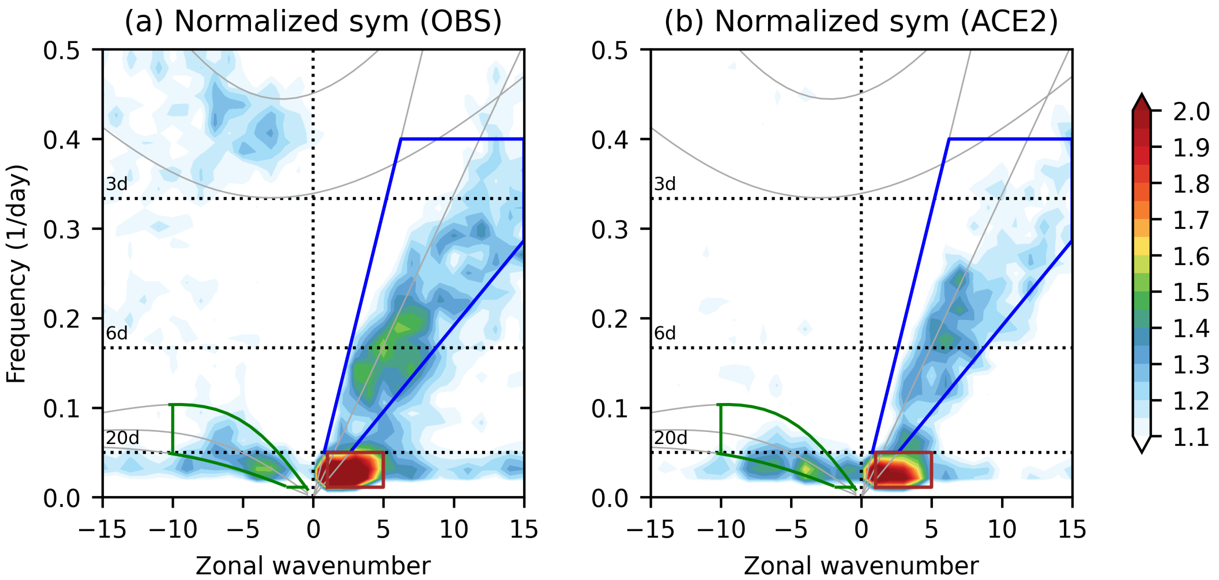

Figure 8. Normalized power spectrum of the symmetric component of precipitation anomalies averaged between 15S and 15N in (a) observation and (b) ACE2 (Simulation I). Horizontal lines indicate 3 days, 6 days, and 20 days. The grey lines indicate the dispersion curves for convectively coupled Kelvin waves (straight lines in positive wavenumber regime), equatorial Rossby waves (curved lines in negative wavenumber regime, with a period longer than ten days), and inertial gravity waves (curved lines across positive and negative wavenumber regime, with a period shorter than 3 days), with the equivalent depth of 8m, 25m, and 90 m. The colored boxes indicate each type of convectively coupled equatorial wave, the blue polygon indicates convectively coupled Kelvin waves, the red box indicates Madden Jullian Oscillation, and the green shape indicates equatorial Rossby wave.

IOP Publishing
Machine Learning: Earth
Journal **XX** (XXXX) XXXXXX
https://doi.org/XXXX/XXXX

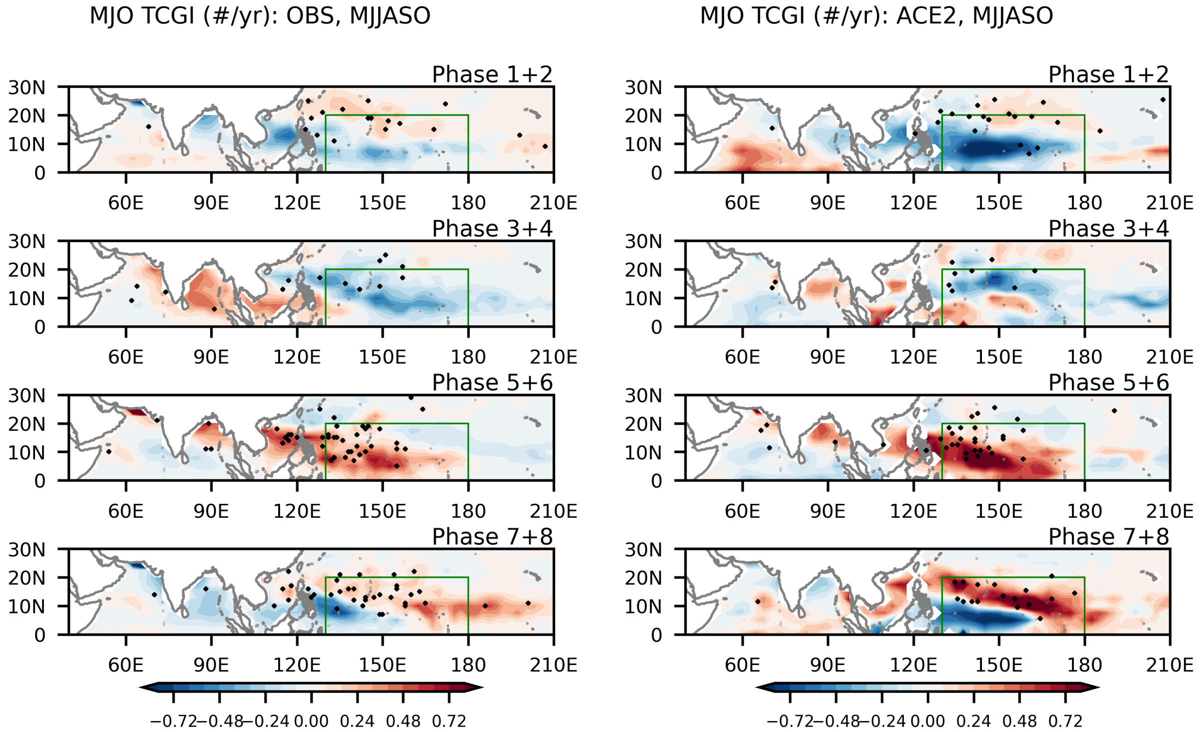

Figure 9. MJO composite of TC genesis index (shading) and actual TC genesis (black dots) in (left) observation and (right) ACE2 (Simulation I) from May to October. Green boxes outline the Western Pacific domain used in Fig. 11.

IOP Publishing Machine Learning: Earth
Journal **XX** (XXXX) XXXXXX https://doi.org/XXXX/XXXX

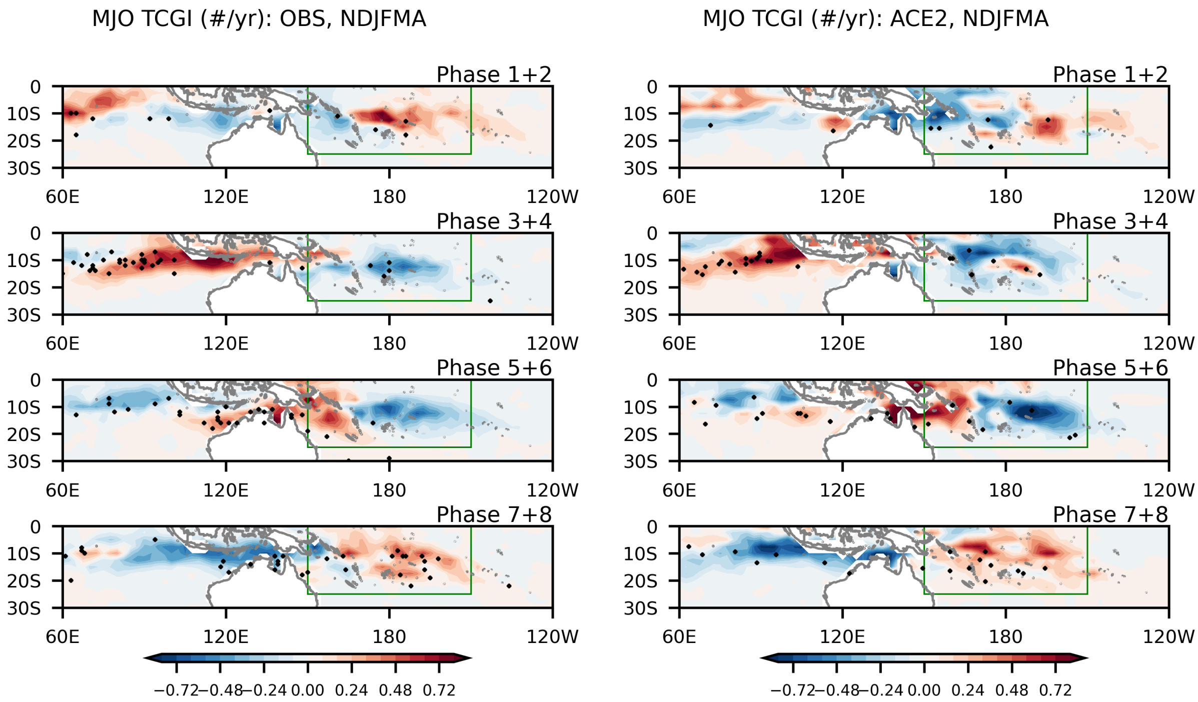

Figure 10. MJO composite of TC genesis index (shading) and actual TC genesis (black dots) in (left) observation and (right) ACE2 (Simulation I) from November to April. Green boxes outline the Southern Pacific domain used in Fig. 11.

IOP Publishing Machine Learning: Earth
Journal **XX** (XXXX) XXXXXX https://doi.org/XXXX/XXXX

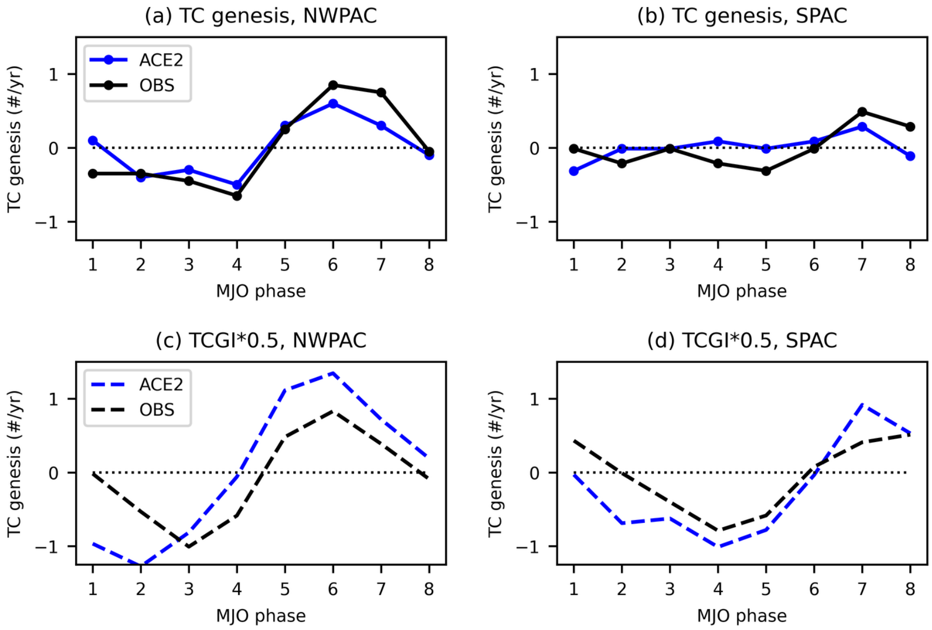

Figure 11. MJO modulation of TC genesis (solid line) and TCGI in (a-b) the North Western Pacific and (c-d) the Southern Pacific Ocean. (left, a, c) observation and (right, b, d) ACE2 (Simulation I).

IOP AI: Earth

Supporting Information for

Modulation of tropical cyclogenesis on subseasonal-to-interannual timescales in the deep-learning climate emulator ACE2

Mu-Ting Chien[1*], Elizabeth A. Barnes[1], and Eric D. Maloney[1]

[1]Department of Atmospheric Science, Colorado State University, Fort Collins, USA

Contents of this file

Figures S1 to S14

Introduction

The supporting information contains fourteen figures that are supplementary to the main results.

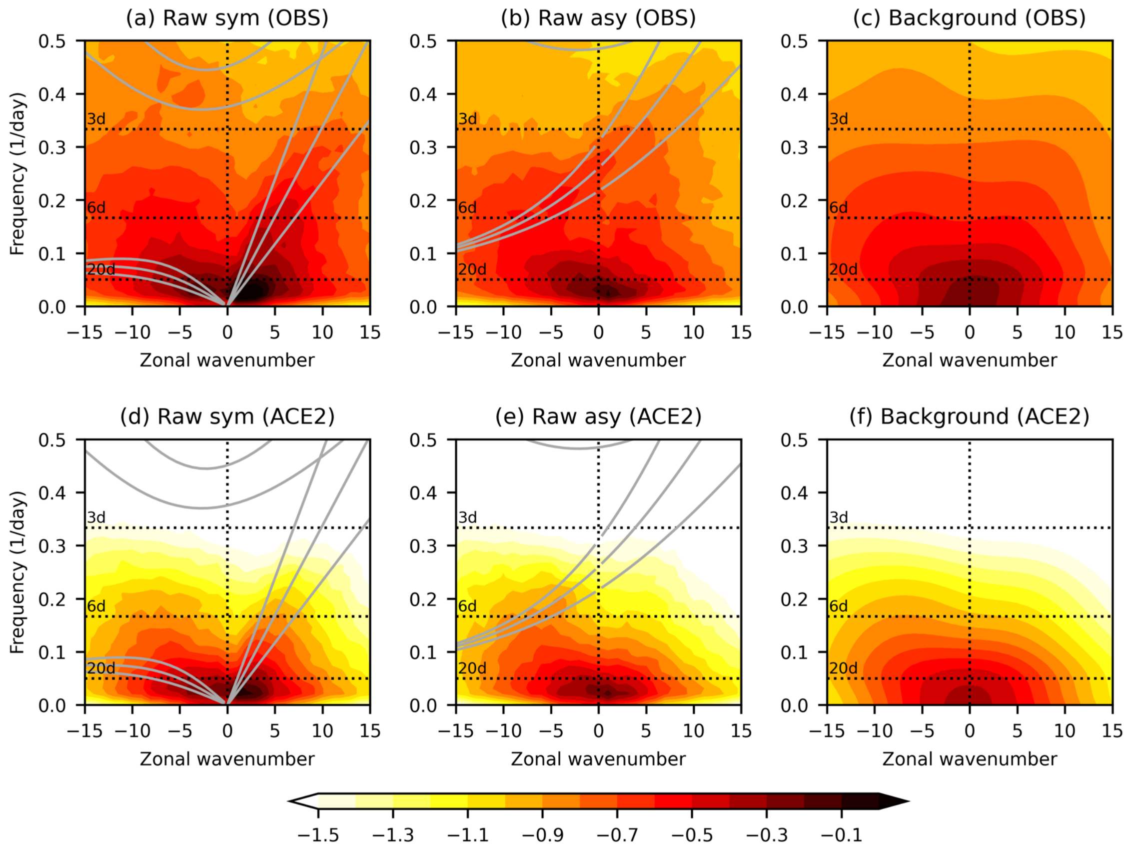

Figure S1. Power spectrum of precipitation anomalies. (a, d): Raw spectrum of symmetric component, (b, e): Raw spectrum of antisymmetric component, (c, f): Background spectrum. The top panel (a-c) shows the IMERG observation, and the bottom panel (d-f) shows the ACE2 simulations (Simulation I).

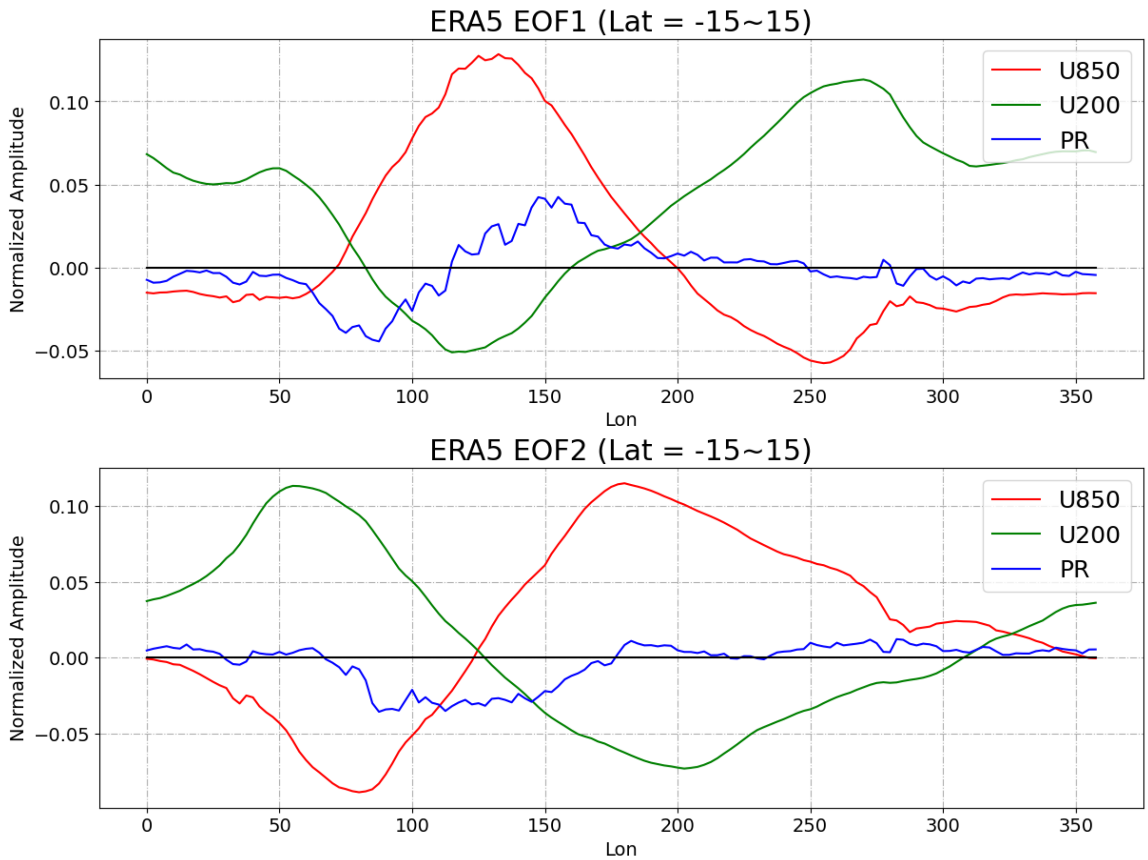

Figure S2. EOFs of the MJO zonal structure obtained from ERA5 reanalysis and IMERG precipitation.

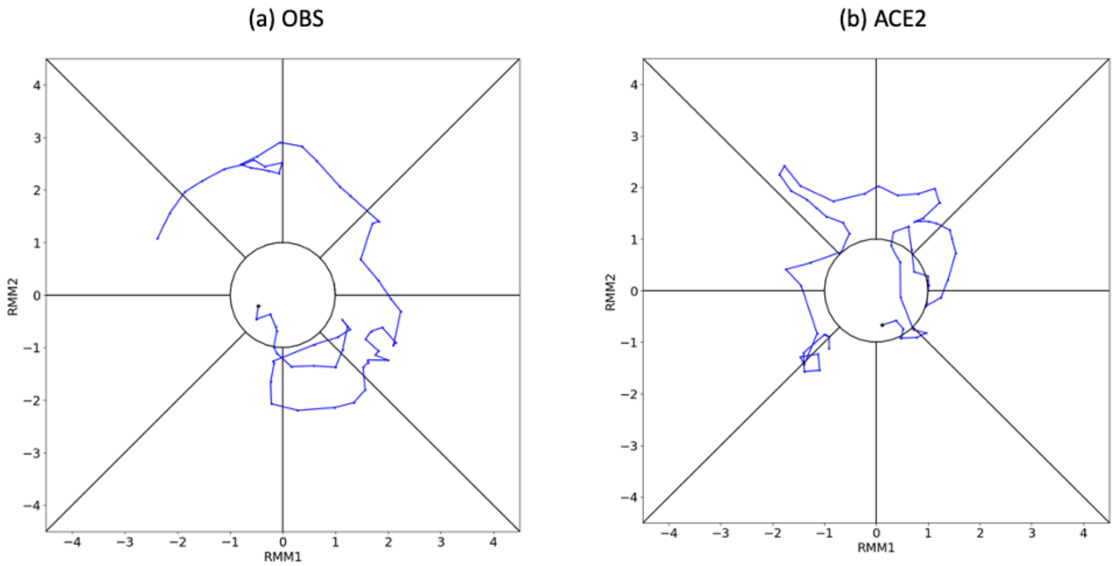

Figure S3. RMM phase diagram for (a) observation and (b) ACE2 (Simulation I). We only show the first 60 days as an example.

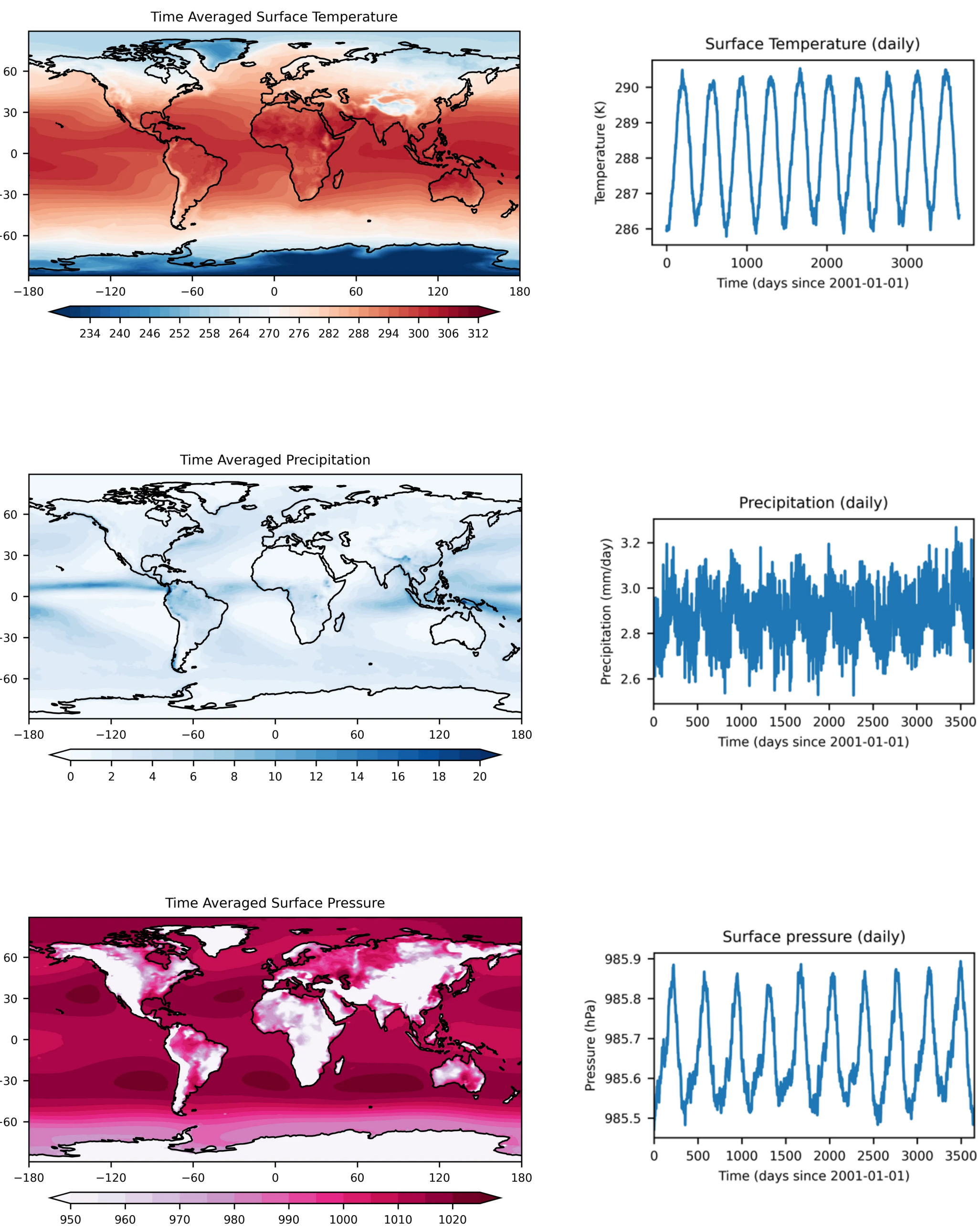

Figure S4. (Left) Mean state (top) surface temperature, (middle) precipitation, and (bottom) surface pressure of our ACE2 simulations (Simulation I). (Right): Global mean time series of each variable from our ACE2 simulations (Simulation I).

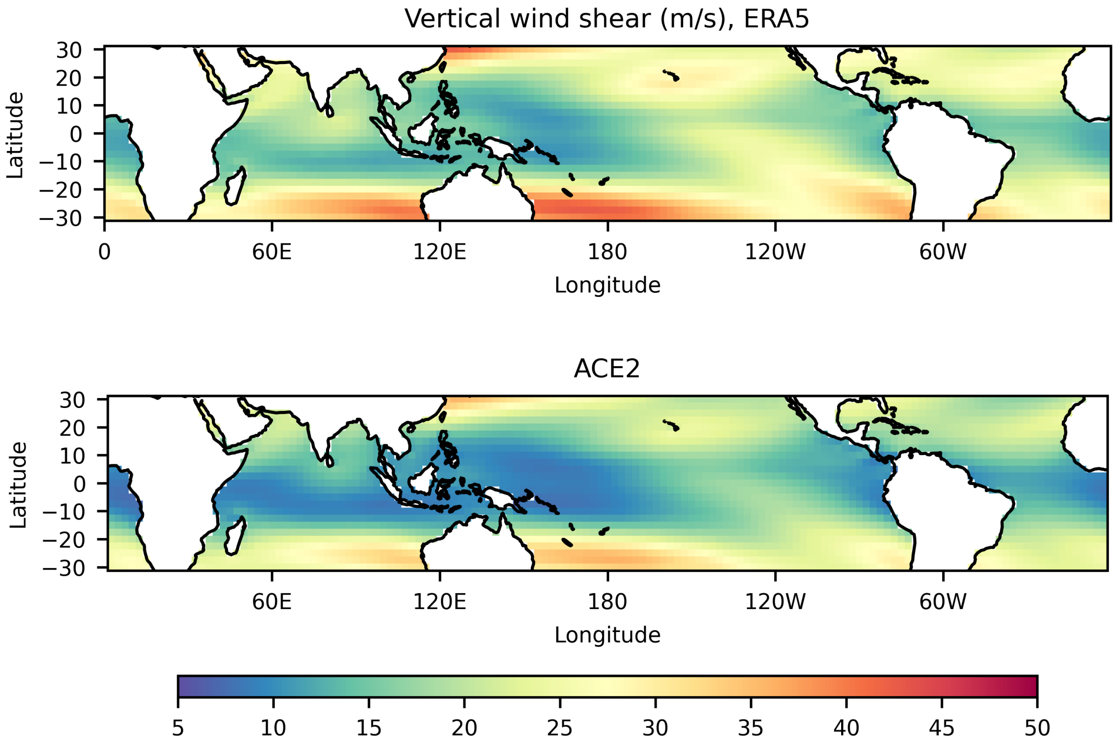

Figure S5. Climatology of vertical wind shear between 850 hPa and 200 hPa in ERA5 (top) and ACE2 (Simulation I) (bottom). The vertical wind shear is used to calculate TCGI.

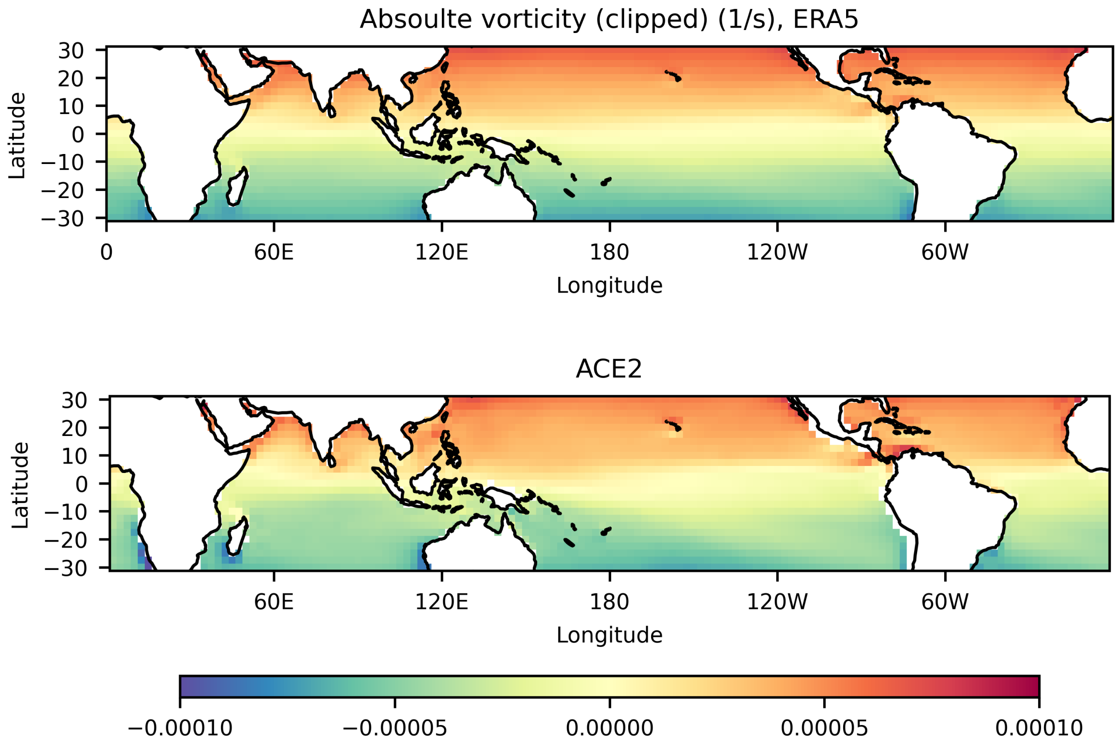

Figure S6. Climatology of absolute vorticity at 850 hPa in ERA5 (top) and ACE2 (Simulation I) (bottom). The absolute vorticity is no smaller than 3.7*$* 10^{-5}$ $1/s$, used to calculate TCGI.

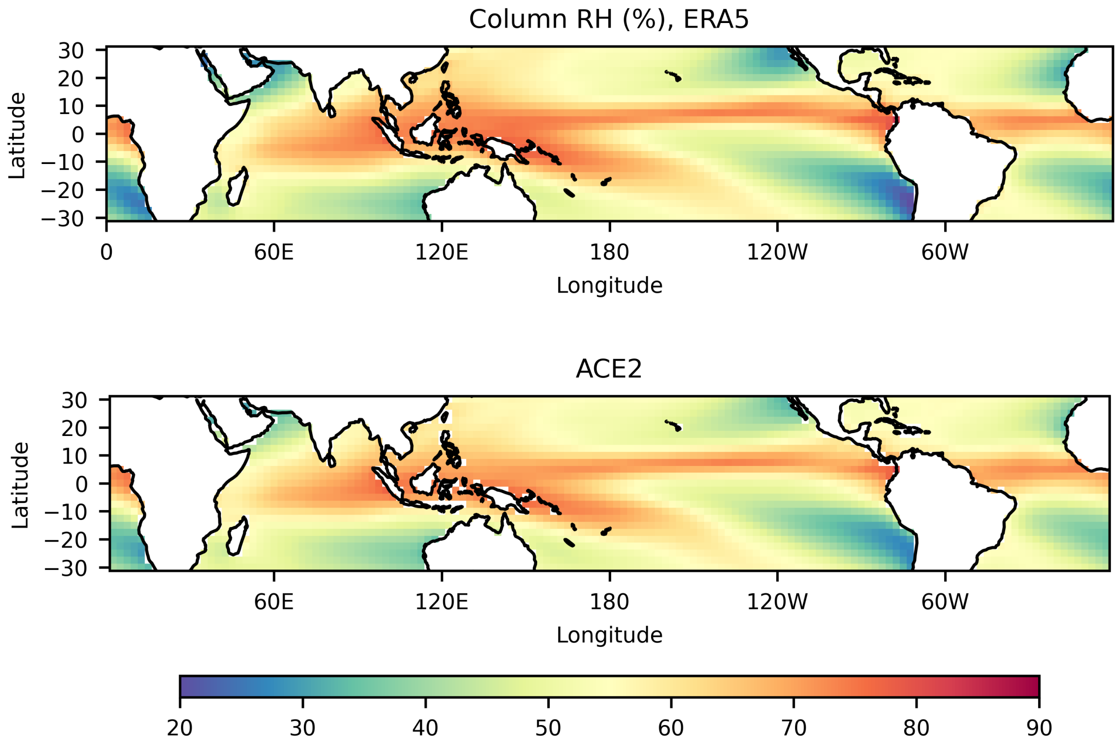

Figure S7. Climatology of column relative humidity in ERA5 (top) and ACE2 (Simulation I) (bottom), used to calculate TCGI.

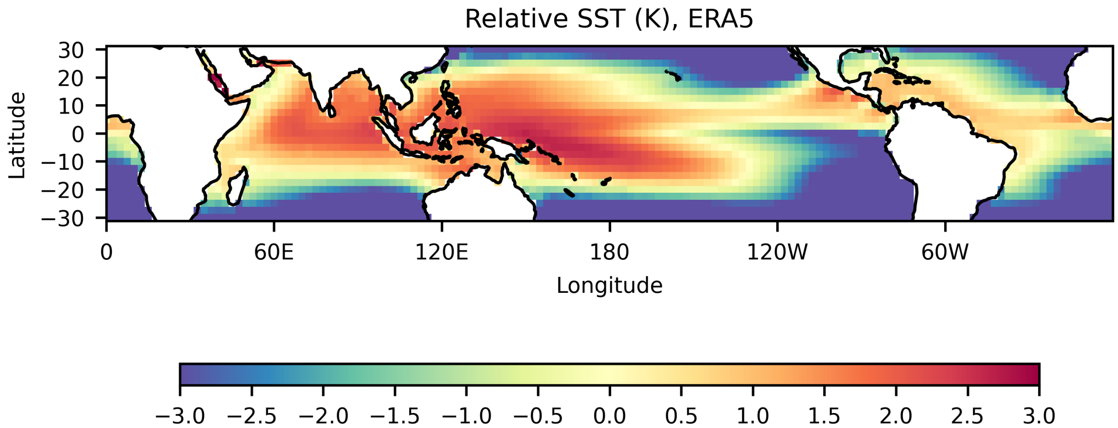

Figure S8. Climatology of sea surface temperature anomalies relative to the tropical mean (20S-20N) in ERA5 and ACE2 (Simulation I). The relative sea surface temperature is used to calculate TCGI. Note that ACE2 is forced by the observed sea surface temperature, and thus, only one SST map is shown.

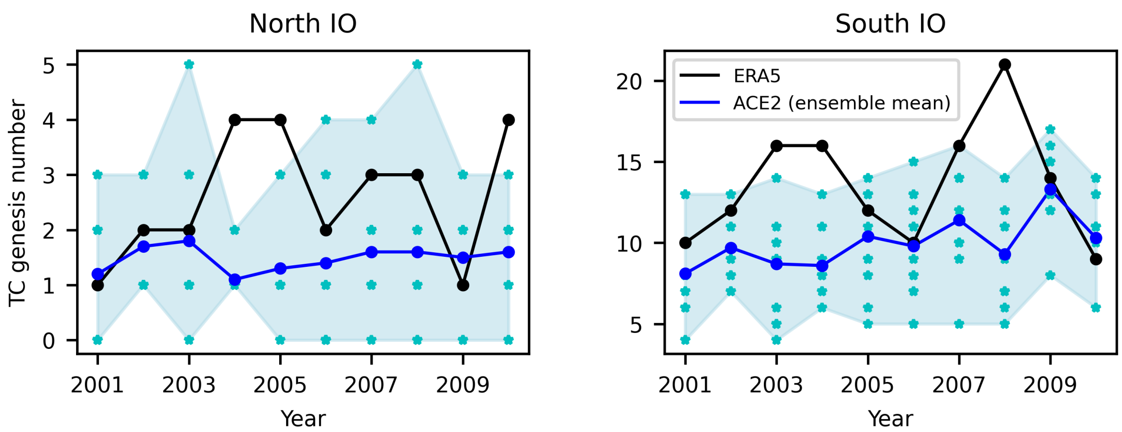

Figure S9. Interannual variability of TC genesis in ERA5 (black line), ACE2 (ensemble mean of Simulation II, dark blue line), and 10 members from ACE2 (Simulation II, light blue stars). Shading represents the ensemble spread. Similar to Fig. 6, but showing only the Northern and Southern Indian Ocean.

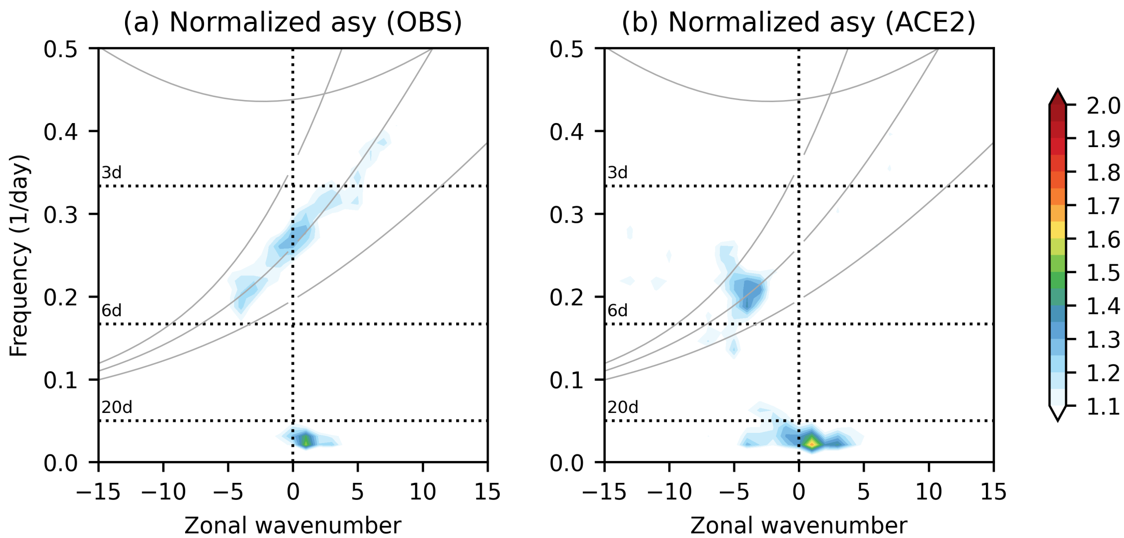

Figure S9. Normalized power spectrum of precipitation anomalies for the anti-symmetric component. The westward propagating wave between 3 to 6 days is the Mixed-Rossby Gravity wave, while the eastward propagating wave between 2.5 to 6 days is the eastward Inertial Gravity wave.

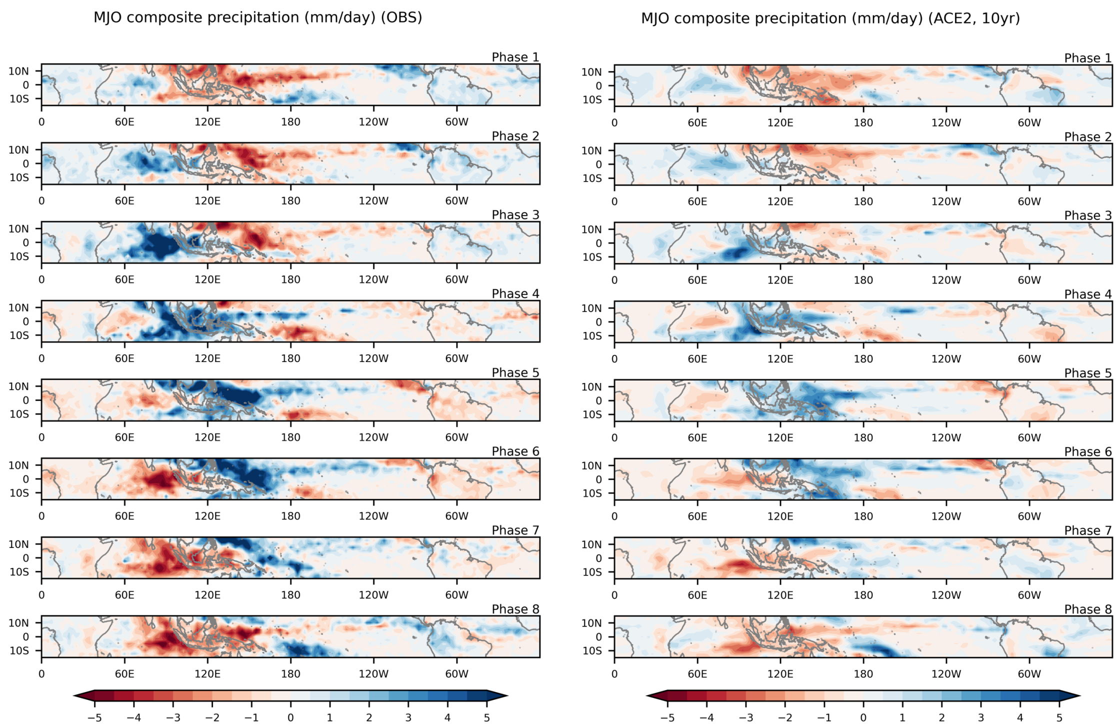

Figure S10. Precipitation anomalies for each MJO phase for all seasons. (Left): observation, (Right): ACE2 (Simulation I).

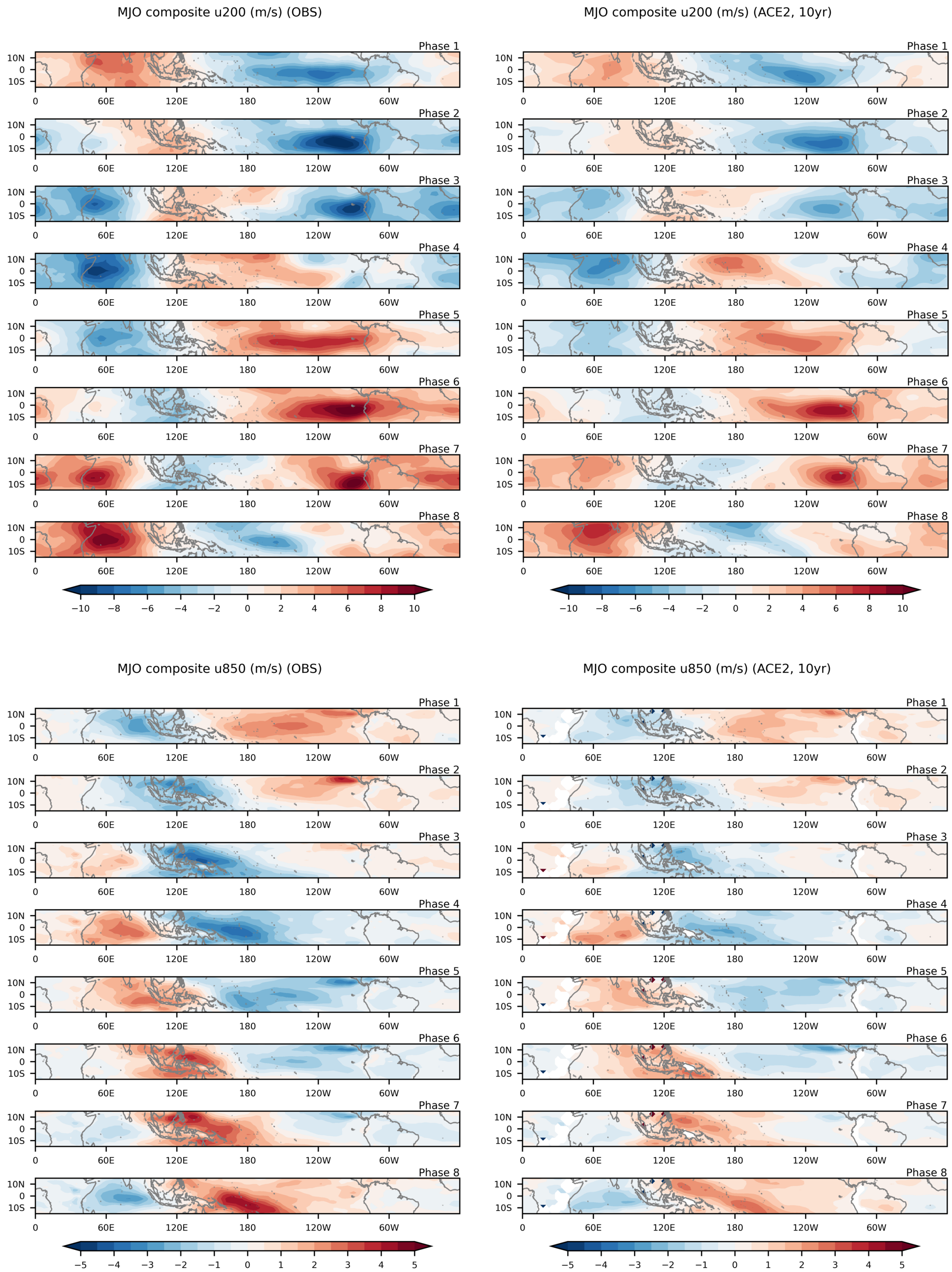

Figure S11. Zonal wind anomalies at (top panel) 200 hPa and (bottom panel) 850 hPa for each MJO phase for all seasons. (Left): Observation, (Right): ACE2 (Simulation I).

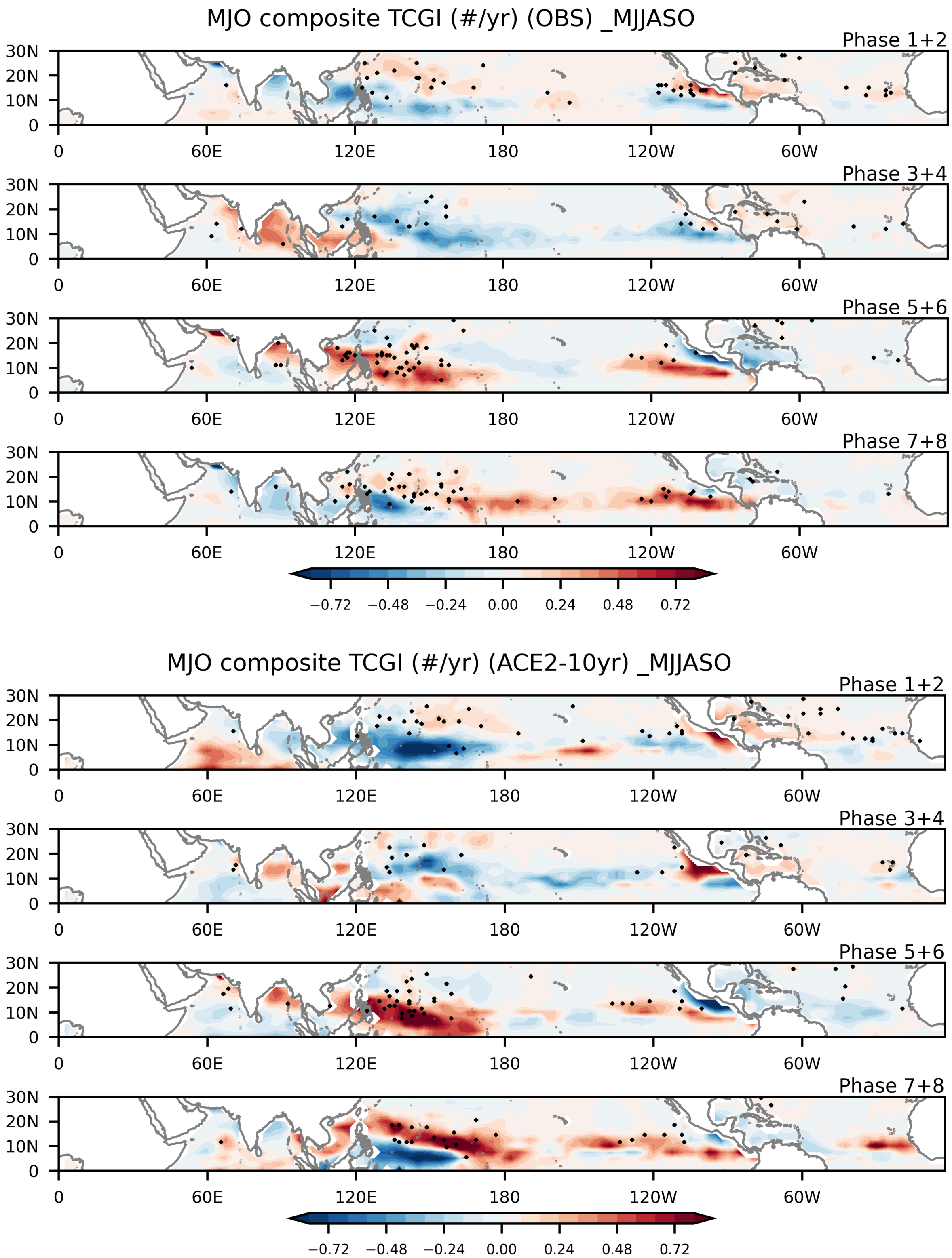

Figure S12. MJO composite of TC genesis index (shading) and actual TC genesis (black dots) in (top) observation and (bottom) ACE2 (Simulation I) from May to October. Similar to Fig. 9, but showing the entire globe.

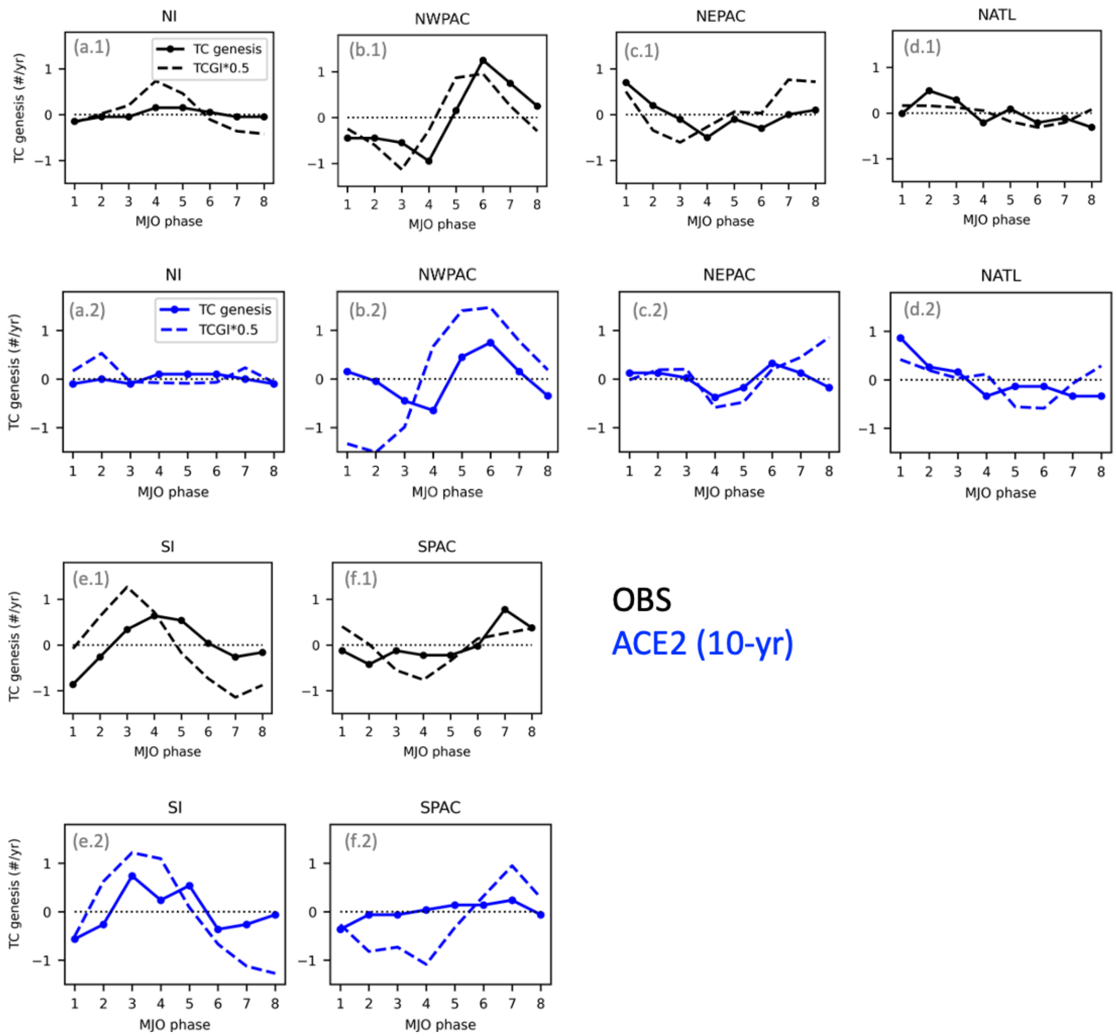

Figure S13. MJO modulation of TC genesis (solid line) and TCGI (dashed line) in all basins. The top panel with black lines shows observation, and the bottom panel with blue lines shows ACE2 (Simulation I).

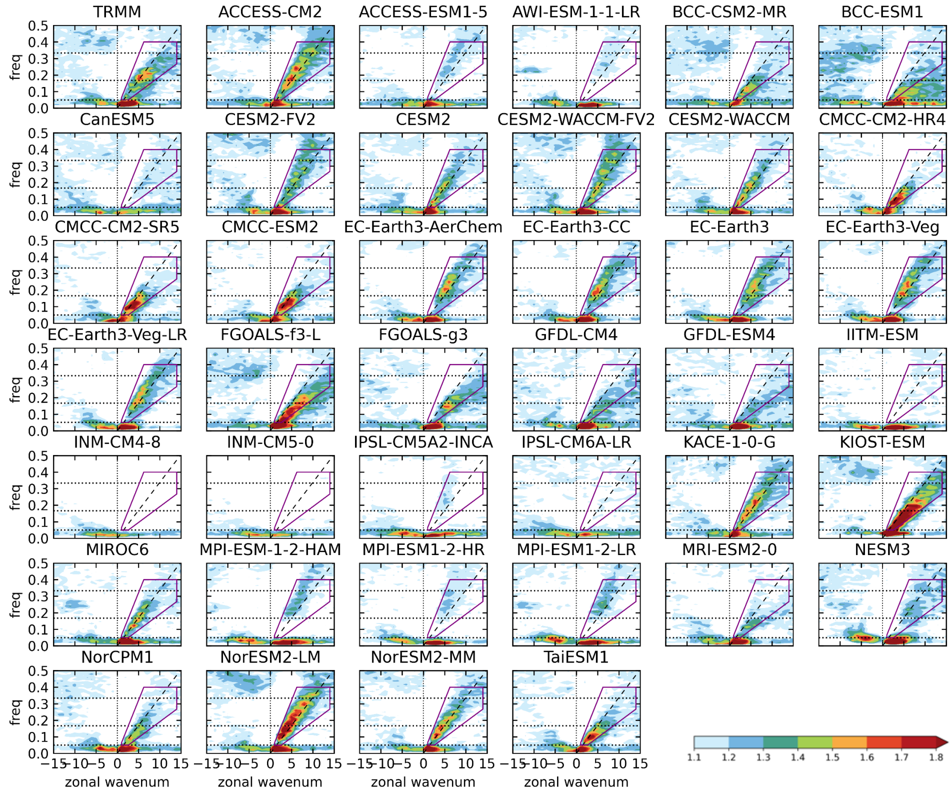

Figure S14. Normalized power spectrum of precipitation anomalies for the symmetric component from the TRMM satellite (top left) and all CMIP6 models (other panels). The Kelvin wave band is indicated in purple polygons.